Paleoceanography and Paleoclimatology

RESEARCH ARTICLE
10.1029/2020PA003960

Silicon Isotopes in an EMIC's Ocean: Sensitivity to Runoff, Iron Supply, and Climate

H. Dietze[1,2], U. Löptien[1,2], R. Hordoir[4,5], M. Heinemann[1], W. Huiskamp[3], and B. Schneider[1]

[1]Institute of Geosciences, Christian-Albrechts University of Kiel, Kiel, Germany, [2]GEOMAR Helmholtz Centre for Ocean Research, Kiel, Germany, [3]Potsdam Institute for Climate Impact Research (PIK), Potsdam, Germany, [4]Institute of Marine Research, Bergen, Norway, [5]Bjerknes Centre for Climate Research, Bergen, Norway

Key Points:
- We simulate the isotopic composition of biogenic silica archived in the ocean's sediment
- Our simulations with an Earth System Model compare modern climate to glacial conditions
- Out of several hypotheses tested, altering the isotopic composition of runoff during the LGM is most consistent with proxies

Correspondence to:
H. Dietze,
heiner.dietze@ifg.uni-kiel.de

Citation:
Dietze, H., Löptien, U., Hordoir, R., Heinemann, M., Huiskamp, W., & Schneider, B. (2020). Silicon isotopes in an EMIC's ocean: Sensitivity to runoff, iron supply, and climate. *Paleoceanography and Paleoclimatology*, *35*, e2020PA003960. https://doi.org/10.1029/2020PA003960

Received 27 APR 2020
Accepted 9 SEP 2020
Accepted article online 14 SEP 2020

Abstract The isotopic composition of Si in biogenic silica (BSi), such as opal buried in the oceans' sediments, has changed over time. Paleorecords suggest that the isotopic composition, described in terms of δ^{30}Si, was generally much lower during glacial times than today. There is consensus that this variability is attributable to differing environmental conditions at the respective time of BSi production and sedimentation. The detailed links between environmental conditions and the isotopic composition of BSi in the sediments remain, however, poorly constrained. In this study, we explore the effects of a suite of offset boundary conditions during the Last Glacial Maximum (LGM) on the isotopic composition of BSi archived in sediments in an Earth System Model of intermediate complexity (EMIC). Our model results suggest that a change in the isotopic composition of Si supply to the glacial ocean is sufficient to explain the observed overall low(er) glacial δ^{30}Si in BSi. All other processes explored trigger model responses of either wrong sign or magnitude or are inconsistent with a recent estimate of bottom water oxygenation in the Atlantic Sector of the Southern Ocean. Caveats, mainly associated with generic uncertainties in today's pelagic biogeochemical modules, remain.

1. Introduction

Numerical, model-based projections into our warming future suggest ensuing global-scale redistribution of nutrients from the sunlit surface ocean to depth. Among the prospective consequences are declining biological productivity and fish yields. Disconcertingly, these effects may prevail for a millennium (Moore et al., 2018). But how reliable are such climate projections?

The problem is that we will not live to calculate substantiated statistics on the reliability of climate forecasts. Hence, an approach similar to the one pursued in weather forecasting, where progress has been accomplished during decades of daily forecasts and subsequent ground truthing (cf. Bauer et al., 2015), is not viable—if pressing societal questions are to be answered in time. A straightforward and generic way to deal with this problem is to assume that fidelity of nowcasts is correlated with the fidelity of climate forecasts. This assumption, however, has been challenged, for example, by Knutti et al. (2009) and Notz (2015) for coupled ocean-atmosphere models and, recently, by Löptien and Dietze (2017, 2019) for models of pelagic biogeochemical cycling.

A potential solution to this dilemma is the assessment of past climate states to test the sensitivity of climate models (as suggested by, e.g., Braconnot et al., 2012). The idea being that the geologic records of environmental responses to past climate changes complement the climate observations from the past decades such that respective fidelity metrics become indicative of the reliability of future projections.

In this regard, the isotopic composition (δ^{30}Si) of biogenic silica (BSi) preserved in ocean sediments is of special interest to the field of pelagic biogeochemical ocean modeling. The reasons are as follows: first, silicic acid (DSi) is an essential element for diatoms, which are autotrophic key players in the pelagic carbon cycle. Second, the isotopic composition of BSi is stable and preserves over millennia once secluded from processes at the water-sediment interface. Third, diatoms produce BSi with a δ^{30}Si distinctly different from the δ^{30}Si of their substrate DSi. The latter is caused by diatoms which tend to build more isotopically light BSi into their shells, compared to the δ^{30}Si in ambient DSi—a process also referred to as fractionation. This fractionation relates the δ^{30}Si of BSi in the sediments to the turnover of DSi by diatoms. The advantage of using the

isotopic composition to improve our current understanding of glacial-interglacial cycles, instead of simply using BSi sediment burial rates, is that δ^{30}Si is less affected by water column processes which are, on the one hand, unrelated to BSi production but may, on the other hand, modulate the amount of BSi that is preserved in the sediments.

A major challenge is the interpretation of δ^{30}Si of BSi records because the link between diatom DSi turnover and δ^{30}Si isotopic signature in BSi is complex (see also Ragueneau et al., 2000). In a (Rayleigh) system, like a surface mixed layer in spring, diatoms preferentially take up lighter DSi until only relatively heavy substrate is left (and subsequently taken up). Hence, the δ^{30}Si isotopic signature in BSi is indicative of the amount of substrate left, with high (low) values indicating oligotrophic (nutrient replete) conditions. In contrast, in a system characterized by high incoming and outgoing physical transports of substrate (e.g., a location within the Gulf Stream) the δ^{30}Si of BSi is predominantly determined by the δ^{30}Si of the constantly resupplied DSi—and only modestly altered by the respective fractionation during BSi production because the fractionation signal cannot build up (since it is constantly flushed out of the local system). Both the Rayleigh and the "flushed" system can be described to high precision by simple equations (e.g., Closset et al., 2016, their Equations 1 to 6). The difficulty is in the quantification of the relation between physical transport flushing rate and biotic BSi export out of the sunlit surface ocean—or in other words: the relation between flushing and BSi production needs to be known in order to interpret δ^{30}Si of BSi records. Further complexity is potentially added by variations of the δ^{30}Si composition of DSi feeding the surface waters.

In summary, both local (production and export of BSi, which is affected by local environmental conditions) and remote processes (production and export upstream which affects incoming environmental conditions), determine the isotopic signature of BSi at a given location. This complex entanglement of ocean circulation and biogeochemistry calls for the application of a three-dimensional numerical model to guide the interpretation of δ^{30}Si in observed BSi records. Indeed, the (modern climate) pioneering studies of Wischmeyer et al. (2003) and Gao et al. (2016) illustrated the benefit of using a numerical coupled ocean-circulation biogeochemical model in linking silicon isotopes to silicic acid utilization.

Using models for interpretation in such ways leads, however, to a causality dilemma. Coupled ocean-circulation biogeochemical models rely on a number of assumptions and (often poorly known) model parameters (such as growth/death of phytoplankton and sinking of organic matter to depth). Most of these assumptions and parameters are not well constrained in the sense that different choices may result in an equally good fit to present-day observations—but simultaneously very different projections (e.g., Löptien & Dietze, 2017, 2019). Thus, paleorecords, such as the isotopic composition of BSi preserved in ocean sediments, are of great interest to assess and reduce such uncertainties. At the same time, these model uncertainties complicate the interpretation of simulated past marine biogeochemical cycling in general (e.g., Hülse et al., 2017) and of the isotopic composition of BSi preserved in ocean sediments in particular. An aggravating circumstance is that the observational records are still so sparse (even for present-day δ^{30}Si DSi), such that Hendry and Brzezinski (2014) conclude that the data set is "...inadequate to evaluate mechanisms leading to even the first-order distribution of isotopes of Si in the global ocean."

Even so, a number of very interesting hypotheses, explaining aspects of spatial and temporal variance in δ^{30}Si of BSi records, have been rooted on the available observational records. Among them is the Silicic Acid Leakage Hypothesis which may explain glacial interglacial atmospheric CO_2 changes (SALH; e.g., Brzezinski et al., 2002; Matsumoto et al., 2002, 2014). In the following we outline the basic idea of the SALH as far as the silicic acid is concerned (see, e.g., as concerns its link to glacial interglacial atmospheric CO_2 changes Matsumoto & Sarmiento, 2008): Today's Southern Ocean (SO) retains or traps DSi at the expense of more northward latitudes by a combination of deep and efficient BSi export and meridional overturning. Driven by the strong southern westerly wind belt, deep, nutrient replete waters are brought to the surface at the Antarctic Divergence. The northward branch of the Divergence (which potentially exports DSi from the SO) is efficiently stripped of DSi by phytoplankton. So, by the time the water reaches the Polar Front and the formation sites of Subantarctic Mode Waters (SAMW) and Antarctic Intermediate Waters (AAIW) which spread northward, most of the DSi has been exported as BSi to depth into the southward flowing Circumpolar Deep Water (CDW). The CDW surfaces south of the Polar Front and, hence, the respective DSi is thereby retained in the SO. The SALH postulates that this DSi trapping in the SO was alleviated during glacial times triggered by, for example, enhanced iron supply: The enhanced iron supply and

associated physiological changes may have reduced the Si demands of diatoms, relative to the need of bioavailable nitrogen. Thus, leftover DSi might have leaked into the SAMW and AAIW and thereby could have left the SO. In summary, the SALH assumes that more DSi might have been available outside the SO during glacial times. A straightforward (Rayleigh) conclusion is that the glacial δ^{30}Si was lower (than today) because, according to the above considerations, DSi should have been less limiting relative to nitrogen.

The SALH and its relation to relatively low glacial δ^{30}Si (e.g., Sutton et al., 2018) has, however, been recently challenged by Frings et al. (2016) who concluded, based on a very comprehensive review, that consistent shifts among different ocean basins from low glacial δ^{30}Si to higher interglacial δ^{30}Si (0.5–1‰) may rather have been caused by a respective change in the isotopic composition of land-ocean fluxes of Si.

Our study adds to the ongoing discussion by exploring various hypotheses potentially triggering lower glacial δ^{30}Si in an Earth System Model of intermediate complexity (EMIC). Our modeling approach builds on the pioneering works of Wischmeyer et al. (2003) and Gao et al. (2016) for modern climate and applies our extended model to both the Last Glacial Maximum and modern climate. Specifically, we explore the effects of (1) differences in the Si:N ratios, mimicking alleviated iron limitation during the LGM (Matsumoto et al., 2014), (2) differing winds during the LGM (e.g., Kohlfeld et al., 2013; McGee et al., 2010; Sime et al., 2013), (3) differing Si supply to the ocean during the LGM (Frings et al., 2016), and (4) a differing isotopic composition of Si supplied to the ocean during the LGM (Frings et al., 2016; Opfergelt et al., 2013). The underlying aim is to illustrate the complex entanglement of ocean circulation and biogeochemistry, which determines the isotopic composition of δ^{30}Si of BSi preserved in sediments.

2. Materials and Methods

2.1. Observations

We use the World Ocean Atlas 2009 data to assess our preindustrial (*PI*) simulation. More specifically, we compare against annual mean climatologies of temperature (Locarnini et al., 2010), salinity (Antonov et al., 2010), phosphate (Garcia, Locarnini, Boyer, & Antonov, 2010), and silicate (Garcia, Locarnini, Boyer, & Antonov, 2010).

Silicon isotopic data in seawater (δ^{30}Si of DSi) are put together from data published in Beucher et al. (2008); Beucher et al. (2011); Cardinal et al. (2005); De La Rocha et al. (2011); de Souza, Reynolds, Johnson, et al., 2012; de Souza, Reynolds, Rickli, et al., 2012; Ehlert et al. (2012); Fripiat, Cavagna, Dehairs, et al., 2011; Fripiat, Cavagnam, Savoye, et al., 2011; Fripiat et al. (2012); Grasse et al. (2013); and Reynolds et al. (2006). A binning procedure increased horizontal data coverage: Surface data with a nominal depth of 50 m refer to binning all data within 0–100 m. Abyssal data refer to binning all data within 1,500–2,500 m.

Silicon isotopic data in BSi as preserved in sediment cores are compiled, following Frings et al. (2016), from Brzezinski et al. (2002); De La Rocha et al. (1997, 1998, 2011); Ehlert et al. (2013); Ellwood et al. (2010); Hendry et al. (2016, 2012); Horn et al. (2011); and Pichevin et al. (2009).

2.2. Model

In this study we present numerical simulations with the University of Victoria Earth System Climate Model (UVic ESCM Weaver et al., 2001). We present equilibrium simulations for two distinct climates, the preindustrial year 1800 (PI) and the Last Glacial Maximum (LGM) 21,000 years before present and evaluate the model's distribution of δ^{30}Si of BSi preserved in ocean sediments. UVic ESCM is an intermediate complexity model, featuring a simplified (vertically integrated) atmosphere. In contrast, the ocean dynamics is, although rather coarse, resolved in all three dimensions. The vertical resolution starts with 50 m at the surface of the ocean and gradually coarsens to 500 m in the abyss. The horizontal resolution of all model components (i.e., ocean, land, atmosphere, and sea ice) is 1.8° in meridional and 3.6° in zonal direction. UVic's assets are low computational demands and an extensive number of peer-reviewed studies including the description of LGM and PI equilibrium simulations. Among its drawbacks are a simplified atmosphere and a spatial resolution of the ocean that is coarse compared to, for example, that class of models that underlie the current projections of the Intergovernmental Panel on Climate Change. Our simulations build on two configurations introduced by Brennan et al. (2012) already.

(1) *PI*, which refers to the "Preindustrial Equilibrium Simulation" described in section 3 of Brennan et al. (2012). Briefly summarized, the atmospheric pCO_2 is set to 283.87 ppm and the orbital configurations to those, representative of the year 1800. The initial conditions are those from the 5 Kyr spinup from Brennan et al. (2012).

(2) *LGM*, which refers to the "Last Glacial Maximum Equilibrium Simulation" described in section 4 of Brennan et al. (2012). Briefly summarized, the atmospheric pCO_2 is set to a low 189.65 ppm; the orbital parameters to those representing the conditions at 21 Kyr BP and the surface elevation and albedo on land are adjusted following a reconstruction of Northern Hemisphere land ice (ICE-4G; Peltier, 1994).

The wind forcing during LGM consists of the same prescribed climatology used for the preindustrial simulations in our rather simple ESCM (see Weaver et al., 2001, for details). Admittedly weak dynamic wind feedbacks are parameterized as a function of surface temperature gradients and added to this climatology. The choice of building on a present-day climatology is pragmatic, since the wind conditions during the LGM are discussed controversially (e.g., Kohlfeld et al., 2013; Sime et al., 2013).

2.2.1. Equations for the Si Cycle

For this study we added an explicit and prognostic representation of (1) dissolved silicic acid (DSi), (2) biogenic Si (BSi), (3) that fraction of DSi that is composed of the silicon isotope ^{30}Si ($D^{30}Si$), and (4) that fraction of BSi that is composed of the silicon isotope ^{30}Si ($B^{30}Si$) to the original pelagic biogeochemical module used in Brennan et al. (2012). All prognostic biogeochemical variables C, at a given point in (model) space, are determined following:

$$\frac{\partial C}{\partial t} = T + sms, \tag{1}$$

where T denotes the spatial divergence of diffusive and advective transports. *sms* refers to the source-minus-sinks term. The *sms* terms of the silicon module are adopted from Gao et al. (2016). The convenience of their approach is that the silicon module does not feed back onto the original biogeochemical model (of, in our case, Brennan et al., 2012). Thus, our silicon isotope module is purely diagnostic in the sense that it does not alter the original climate and carbon cycles documented by Brennan et al. (2012) already.

The respective *sms* terms, that describe the linkage of the silicic acid cycle with the pelagic biogeochemical cycle of Brennan et al. (2012), are described below. Approach and notation follow Gao et al. (2016). The DSi is supplied to the ocean at a temporally constant rate, *RRDSi* of 9.55 Tmol Si year^{-1} (Frings et al., 2016) and is homogeneously distributed over the surface ocean.

- *DSi equation:*

$$sms(DSi) = r\,BSi - P_{Si}, \tag{2}$$

where r denotes the diatom opal dissolution rate and P_{Si} denotes the biogenic opal production. r is temperature dependent:

$$r = A\exp(T/T_c), \tag{3}$$

with the parameters A setting the dissolution rate and T_c determining the temperature dependance of opal dissolution. The value of T_c is adopted from Gao et al. (2016; see Table 1). The value of A has been determined in a tuning exercise (see section 2.2.2), P_{Si} is calculated as a function of the production rate of particulate organic matter, *pomp* (as calculated by the original biogeochemical module of Brennan et al., 2012) and DSi concentration:

$$P_{Si} = \min\left(pomp\,R_{Si:P}\frac{DSi}{K_{PHY}^{DSi} + DSi},\ r_{Pro}\,DSi\right), \tag{4}$$

where $R_{Si:P}$ denotes the molecular DSi to phosphate uptake ratio, associated with BSi production, K_{PHY}^{DSi} denotes the half-saturation constant of DSi uptake (see Table 1). r_{Pro} is the maximum rate of BSi production under nonlimiting conditions.

Table 1
Reference Model Parameters of our Implementation of the Gao et al. (2016) Silicon Module into the Pelagic Biogeochemical Module of Brennan et al. (2012)

Parameter	Description	Gao et al. (2016)	Our value	Unit
A	opal dissolution rate	333^{-1}	90^{-1} (see Figure 1)	day^{-1}
T_c	critical temperature of opal dissolution	12	12	°C
$R_{Si:P}$	molecular DSi to phosphate stoichiometric ratio	25	25	$\frac{molDSi}{molP}$
K_{PHY}^{DSi}	half-saturation constant of DSi uptake during BSi production	4	4	$\frac{mmolDSi}{m^3}$
r_{Pro}	BSi production rate under nonlimiting conditions	0.5	0.5	day^{-1}
w	sinking speed of BSi	10	10	$\frac{m}{day}$
RRDSi	total Si supply to the (surface) ocean (by, e.g., river runoff)	9	9.55 (Frings et al., 2016)	$\frac{TmolSi}{year}$
$RR\delta^{30}$	isotopic composition of (riverine) Si supply to the (surface) ocean	0.8	0.74 (Frings et al., 2016)	‰
α_1	^{30}Si fractionation factor during BSi production	0.9989	0.9989	[]
[]	fractionation factor during BSi dissolution	1	1	[]

- *BSi equation*:

$$sms(BSi) = -rBSi + P_{Si} - w\frac{\partial BSi}{\partial z}, \tag{5}$$

where w is the sinking speed of BSi and $w\frac{\partial BSi}{\partial z}$ denotes the divergence of vertical BSi fluxes.

- *$D^{30}Si$ equation:*
  Following Gao et al. (2016), we include, in addition to total Si (i.e., the sum of the stable isotopes ^{28}Si, ^{29}Si, and ^{30}Si), an explicit representation of the silicon isotope ^{30}Si. During BSi production, we apply the fractionation factor $\alpha_1 = 0.9989$ (De La Rocha et al., 1997; Gao et al., 2016) which reduces the uptake of heavier ^{30}Si relative to the lighter Si stable isotopes.

$$sms(D^{30}Si) = rBSi\frac{B^{30}Si}{BSi} - P_{Si}\alpha_1\frac{D^{30}Si}{DSi}. \tag{6}$$

Following Gao et al. (2016), we assume no fractionation during BSi dissolution.

- *$B^{30}Si$ equation:*

$$sms(B^{30}Si) = -rBSi\frac{B^{30}Si}{BSi} + P_{Si}\alpha_1\frac{D^{30}Si}{DSi} - w\frac{\partial B^{30}Si}{\partial z}. \tag{7}$$

We calculate the silicon isotopic composition $\delta^{30}Si$ in units of ‰ as a function of the total DSi (or BSi) concentration and D^{30}Si (or B^{30}Si) following:

$$\delta^{30}Si = \left(\frac{(^{30}Si/^{28}Si)_{sample}}{(^{30}Si/^{28}Si)_{NBS-28}} - 1\right)\cdot 10^3, \tag{8}$$

$(^{30}Si/^{28}Si)_{NBS-28} = 0.0335$ (Coplen et al., 2002). We calculate ^{28}Si from the total Si and ^{30}Si concentrations as $^{28}Si = 0.953(Si - ^{30}Si)$ which assumes that all stable isotopes other than the ^{28}Si and ^{30}Si always amount to 4.7% of total Si. (Here we follow Reynolds, 2009, stating that the assumption of a constant relative abundance of the normalizing isotope "...is valid for small isotopic variations described by the δ notation".) We set the isotopic composition $\delta^{30}Si$ of DSi supplied to the surface ocean (mimicking, e.g., river runoff) $RR\delta^{30}$ to 0.74 (Frings et al., 2016).

Our implementation of processes in the sediments is idealized. Once BSi sinks out of the lowermost wet model grid box, it gets buried and leaves the system forever. A constant surface flux RRDSi (Table 1) replenishes what is lost by sedimentation—if the integration is long enough so that the model can reach an equilibrium. Simulated $\delta^{30}Si$ of sedimented BSi are taken as the simulated isotopic composition of BSi sinking out of the lowermost wet model grid box. This idealization is motivated by the urge to save computational resources that would otherwise be necessitated to equilibrate the sediment model.

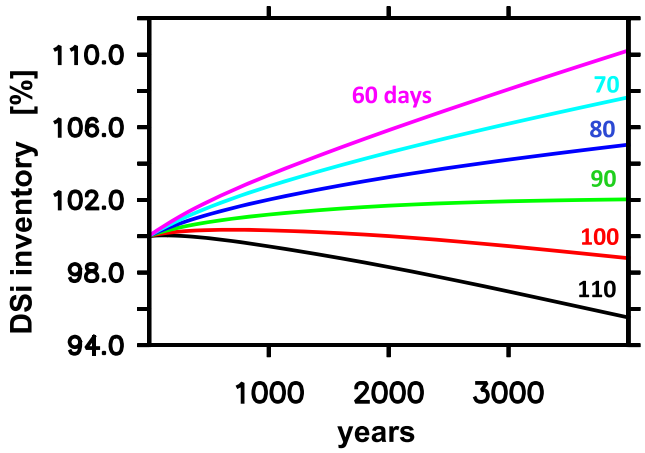

Figure 1. Temporal evolution of simulated preindustrial oceanic DSi inventory relative to observations (WOA09 Garcia, Locarnini, Boyer, & Antonov, 2010; also used to initiate the model) in units of %. The different colors denote simulations with different opal dissolution rates (i.e., different choices of parameter A in Table 1). The colored numbers denote the respective inverse of parameter A in units of days.

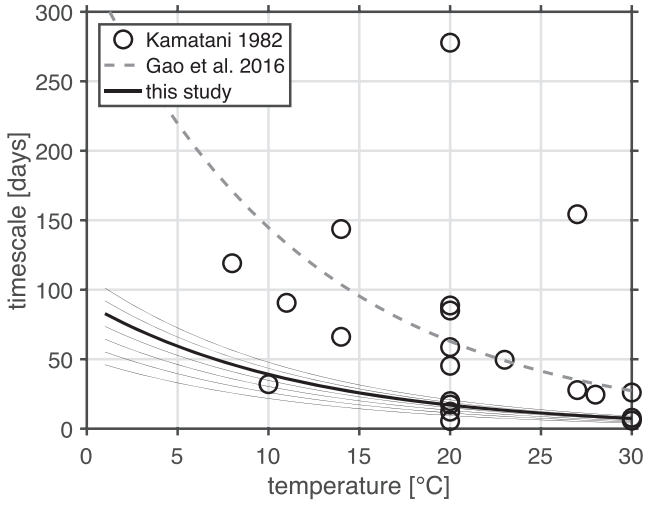

Figure 2. Inverse of dissolution rates of silica from diatoms as a function of ambient temperature. The circles denote data compiled by Kamatani (1992). Three values in excess of 300 days have been discarded here. The dashed gray line refers to settings in the model of Gao et al. (2016). The thick black line refers to the reference model setting in this study. The thin thick lines refer to settings tested during tuning the DSi inventory.

2.2.2. Parameter Settings

The volume of the ocean is $1.4 \cdot 10^{18}$ m^3, containing an average DSi concentration of 92 mmol Si m^{-3} (Garcia, Locarnini, Boyer, & Antonov, 2010). This yields an oceanic inventory of $1.3 \cdot 10^{17}$ mol Si. Division of the inventory with the supply rate of DSi (RRDSi; Table 1) to the ocean yields a timescale of 14,000 years. This timescale is a rough estimate of the residence time of DSi in the ocean consistent with the 9,000 to 16,000 year range estimated by Georg et al. (2009) and Tréguer et al. (1995), respectively. The residence time of DSi provides a lower bound on the time our model framework needs to adjust to changes to the formulation of Si cycling. It is a measure of the expected equilibration timescale of the model.

The long equilibration timescale of our Si module calls for long wall clock times until the effects of model changes can be evaluated reliably. This limits the number of model parameters (and formulations) that can be explored. Our approach here is to use the original model formulations and parameters from Gao et al. (2016) and to adjust only the opal dissolution rate A, such that the DSi inventory stays close to the observations from Garcia, Locarnini, Boyer, and Antonov (2010). Figure 1 shows that, to this end, the choice of $A = 90^{-1}$ $days^{-1}$ is the best compromise between fast equilibration (which saved wall clock time) and small misfit to observations (only 2% overestimation of DSi inventory) among the choices of A tested in this study.

Figure 2 shows the temperature dependance of silica dissolution rates that is associated with our choice of A: Compared with Gao et al. (2016), our choice features substantially faster dissolution rates, throughout the entire range of temperatures. When compared to data compiled by Kamatani (1992), it is, however, still consistent with observations. On these grounds we justify our choice of $A = 90^{-1}$. We provide a respective model assessment for the Si module in Appendix A1.

2.2.3. Experiments

As outlined above (section 2.2), we run our reference model version under PI and LGM climate conditions to quasi-equilibrium (simulations *PI* and *LGM*). In a second step, starting from *LGM*, we perform a suite of sensitivity experiments for the LGM. Table B1 lists these experiments, tailored to explore the sensitivity of our model toward environmental changes. The focus is on changes that have been suggested in the literature to have engrained substantial signatures in the isotopic composition of δ^{30}Si of the BSi archived in oceanic sediments. These simulations are setup as follows:

- *LGMfe* is designed to mimic the effect of iron replete conditions on DSi uptake. As summarized by Matsumoto et al. (2014), there is evidence from incubation experiments that the Si:N consumption ratio is high under iron-depleted conditions (Franck et al., 2000; Hutchins & Bruland, 1998) and relatively low under iron replete conditions (Franck et al., 2000; Pondaven et al., 2000). In experiment *LGMfe* the molecular DSi to phosphate stoichiometric ratio $R_{Si:P}$ is reduced by 36%. Because the N:P ratio is fixed to 16 in our model, this corresponds to a Si:N ratio of 1.
- *LGMbreezy* and *LGMslack* are designed to test the effect of potential glacial interglacial variability of climatological winds driving the ocean circulation: The wind conditions during the LGM remain poorly constrained, such that even the sign of changes relative to today's

conditions is uncertain (e.g., Kohlfeld et al., 2013; McGee et al., 2010; Sime et al., 2013). In order to envelope the range of potential effects on δ^{30}Si of BSi, we follow Matsumoto et al. (2014) and test both a global doubling of wind speeds and a halving, dubbed *LGMbreezy* and *LGMslack*, respectively. These changes affect only the momentum received by the ocean.

- *LGMflush* and *LGMtrickle* are designed to test the effect of potential glacial interglacial variability of riverine Si inputs into the ocean. Following Frings et al. (2016), who suggest, based on a literature review, that the river DSi flux has been within ±20% of today's inputs during the LGM, we increase (decrease) the total supply of Si to the surface ocean by 20% in experiment *LGMflush* (*LGMtrickle*). Because reliable data regarding the variability of the spatial distribution of this input over time are sparse, we distribute all input evenly over space.
- *LGMlight* is designed to test the idea of Frings et al. (2016) that the relatively low values of δ^{30}Si archived in glacial BSi are caused by an isotopically lighter composition of riverine Si inputs to the ocean. Following Frings et al. (2016), *LGMlight* reduces the δ^{30}Si of DSi supplied to the ocean by 1‰. The underlying idea is that biotic and abiotic processes acting along the course of a river determine the isotopic composition of the runoff to the ocean. To this end, the study of Schoelynck et al. (2019) is an illustrative curiosity showing the effect of a single herd of hippos increasing δ^{30}Si by a sizable 0.2‰ in Mara River, Kenya. Further, there is evidence that the isotopic composition of groundwater inputs (Georg et al., 2009) and glacial meltwaters (Hawkins et al., 2018) may also have changed over glacial-interglacial cycles (Georg et al., 2009).

2.3. Manifestation Timescales

Our model investigations are all based on numerical time slice experiments (i.e., we run the model to quasi-equilibrium under the respective boundary conditions)—as opposed to investigating transient responses. Such an approach discards the information regarding the timescales on which model responses to disturbances manifest themselves. This may spuriously illuminate links between processes and their manifestation in the isotopic composition of material archived in sediment cores. We thus measure "manifestation timescales" by locally fitting exponential functions to the simulated δ^{30}Si anomalies in BSi of the 10,000 year sensitivity experiments, listed in Table 2. Depending on the sign of changes in δ^{30}Si in BSi, we fit either to

$$f(t, x, y) = \alpha(x, y)e^{-\frac{t}{\tau(x, y)}} \tag{9}$$

or

$$f(t, x, y) = \alpha(x, y)\left(1 - e^{-\frac{t}{\tau(x, y)}}\right), \tag{10}$$

where $f(t, x, y)$ is the accumulated change in δ^{30}Si of BSi at time t, longitude x, and latitude y. The constant $\alpha(x, y)$ and the manifestation timescale $\tau(x, y)$ are estimated by using an unconstrained nonlinear minimization of the root-mean-square deviation between the local exponential fit and simulated local changes in δ^{30}Si in BSi (Nelder-Mead, described in, e.g., Lagarias et al. (1998), starting with an initial guess of $\tau = 100$ years and $\alpha(x, y)$ as the difference of δ^{30}Si anomalies between the start and the end of respective time slice experiments.

3. Results

In the following subsections we explore the results of the sensitivity experiments regarding their ability to reproduce observed differences in the δ^{30}Si signature between LGM and PI. Each of the sensitivity experiments builds on a scenario of environmental LGM conditions proposed earlier in the literature (see section 2.2.3 and Table 2). The major aim is to dissect mechanisms that lead to reasonable agreement with the observations and paleoarchive data.

3.1. LGM

Figure 3a shows the difference between the LGM "reference" simulation *LGM* and our preindustrial simulation *PI*. We find that the colder glacial climate, overall, increases δ^{30}Si of BSi deposited to the sediments (relative to PI). This is inconsistent with observations typically featuring lower glacial δ^{30}Si. (An exception

Table 2
Model Simulations

Tag	Description	Initial conditions	Duration of simulation
PI	"Preindustrial Equilibrium Simulation" of Brennan et al. (2012)	equilibrated simulation of Brennan et al. (2012)	10,000 years
LGM	"Last Glacial Maximum Equilibrium Simulation" of Brennan et al. (2012)	equilibrated simulation of Brennan et al. (2012)	20,000 years
LGMfe	identical to *LGM* except for Si:N stoichiometric ratio reduced to 1, mimicking the effect of iron replete conditions	end of *LGM*	10,000 years
LGMbreezy	identical to *LGM* except for a doubling in all winds, driving the oceanic circulation	end of *LGM*	10,000 years
LGMslack	identical to *LGM* except for a halving of all winds, driving the oceanic circulation	end of *LGM*	10,000 years
LGMflush	identical to *LGM* except for 20% increase in land-ocean DSi supply	end of *LGM*	10,000 years
LGMtrickle	identical to *LGM* except for 20% decrease in land-ocean DSi supply	end of *LGM*	10,000 years
LGMlight	identical to *LGM*except for a 1‰ decrease in δ^{30}Si of land-ocean DSi supply	end of *LGM*	10,000 years

to this rule is the Atlantic Ocean where simulated glacial δ^{30}Si of BSi are lower and roughly consistent with observations.)

In order to set a reference point for the following discussions (in this section), we dissect the processes that imprint the wrong sensitivity into simulation *LGM*: Key to a better understanding is that *LGM* features an oceanic DSi inventory that is 15% lower relative to that in *PI*. This is puzzling because the export of BSi across 120 m depth (which constitutes the origin of all BSi sinking to depth) is also reduced by a substantial 30%

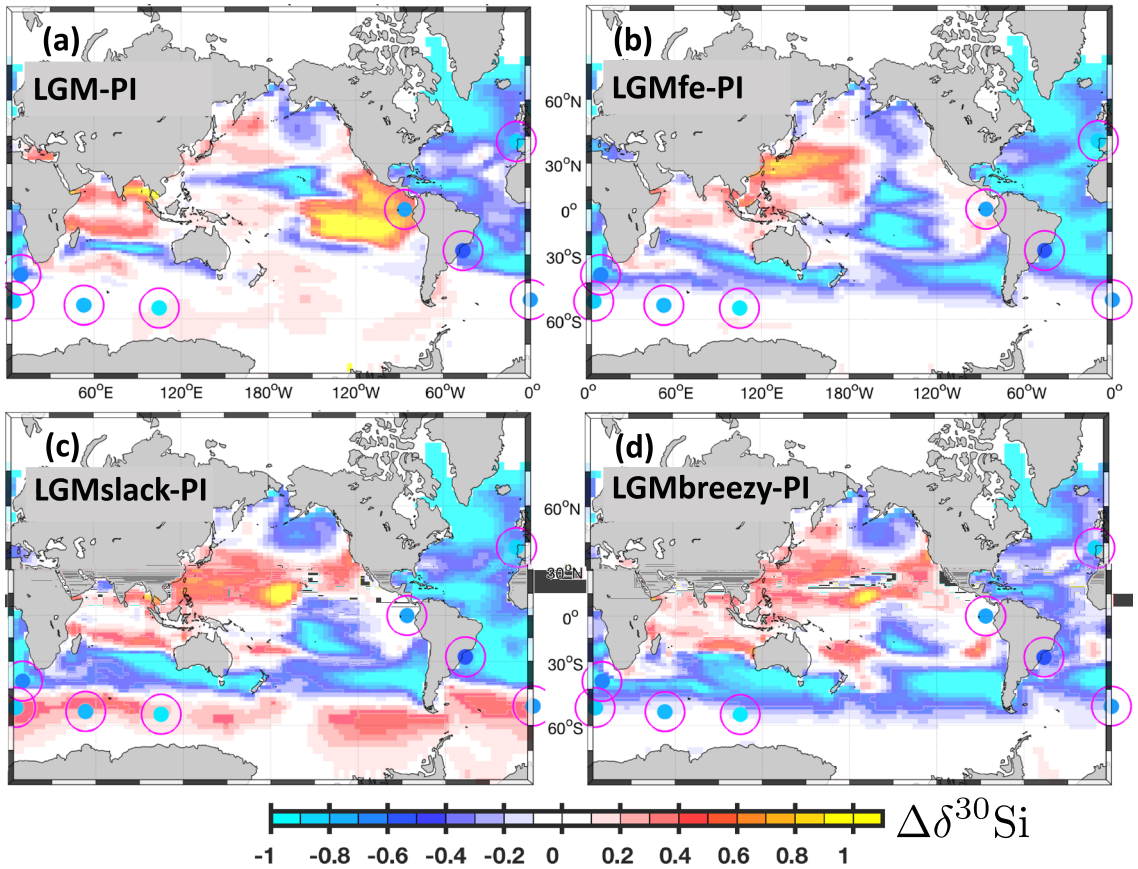

Figure 3. Difference in simulated δ^{30}Si of BSi relative to the preindustrial simulation *PI* as deposited to sediments in units of ‰. Panels (a)–(d) refer to differences *LGM-PI*, *LGMfe-PI*, *LGMslack-PI*, and *LGMbreezy-PI*, respectively. Magenta circles denote locations of observations of δ^{30}Si in BSi as preserved in sediment cores (see section 2.1).

during the colder LGM climate. Given that the riverine supply of Si is identical in *LGM* and *PI*, this is counterintuitive. Further investigations revealed that the process behind this conundrum is the antagonistic effect of temperature on BSi sedimentation rate in our model framework. *LGM* features, consistent with observational evidence (e.g., Members, 2009), an average of 2°C colder oceanic temperature than *PI*. In combination with an increase in sea ice cover during the LGM, which shields the ocean from photosynthetically active radiation essential for autotrophic growth, this slows down the global primary production and associated export of organic material from the sunlit surface to depth. Hence, less BSi is produced and less BSi is set on its way sinking to the sediments. This reduction in BSi production is, however, overcompensated by a remineralization rate that is also slowed down by the lower temperatures such that more organic material reaches the seafloor before it is remineralized and dissolved. A rough scaling, assuming steady state (and horizontal uniformity which reduces the problem to one spatial dimension), puts the potential of this effect into perspective: The vertical flux of sinking BSi described in Equation 5 is, following the notation of Kriest and Oschlies (2008), given by

$$F(z') = F_0 \exp\left(-\frac{rz'}{\overline{w}}\right), \tag{11}$$

where $F(z')$ is the sinking flux at depth z' defined as that distance between actual depth and the depth of the euphotic zone. F_0 is the flux out of the euphotic zone. The sinking speed $\overline{w}$ is 10 m day^{-1} (see Table 1), and r as defined by our Equation 3. For an ocean with a uniform temperature of 4°C Equation 11 (such as in *PI*) yields a sedimentation efficiency (here defined as the ratio between flux to the sediment and export out of the euphotic zone) of 2‰. A reduction of temperature down to 2°C (such as in *LGM*) yields 5‰. Hence, a reduction of only 2°C yields a substantial (initial) 2.5-fold increase in respective sedimentation rates. It is this temperature-driven increase in sedimentation efficiency that reduces the global availability of DSi and, consequently, increases the overall δ^{30}Si in our *LGM* simulation relative to *PI*.

As concerns the decreasing δ^{30}Si of BSi in the Atlantic Ocean, which outweighs the globally reversed trend, we find: North of 55°N the simulated DSi inventory is substantially higher during the LGM, relative to PI (Figure A3). This is owed to fundamentally different global circulation patterns in *PI* and *LGM*. In *PI* the upper branch of the meridional overturning circulation (MOC) supplies the North Atlantic with surface waters that are already relatively depleted in DSi because of biologically induced BSi export from the surface to depth. The lower branch of the MOC exports deep waters enriched in BSi such that the DSi content of the Atlantic Ocean is relatively low. Simulation *LGM* differs in that sea ice protrudes down to 52°N (in winter) which shields respective algae from photosynthetically active radiation. This reduced vertical export of BSi meets throttled MOC (2 Sv versus 18 Sv in the simulation *PI*) which puts an end to the cycle that reduces the DSi inventory of the Atlantic Ocean. The supply of DSi to the surface ocean is identical in *PI* and *LGM*. It has a prescribed, relatively (compared to surface values in the North Atlantic) low δ^{30}Si value of 0.74‰ and is evenly distributed over the ocean in our model (see section 2.2.1). This eventually reduces the δ^{30}Si of BSi in the glacial Atlantic Ocean because it is no longer (or far less) counteracted by the peculiar interplay between biology and MOC described above.

3.2. LGMfe

The simulation *LGMfe* anticipates that more bioavailable iron was available during the LGM. We mimic this effect by reducing the DSi demands by 36% relative to the nitrogen (and phosphorous) demands in our model. This decelerates the biogeochemical cycling of DSi which—according to the Silicic Acid Leakage Hypothesis (SALH)—would reduce the DSi trapping efficiency of the SO. The basic idea behind today's relatively efficient DSi trapping in the SO is that surface waters on their way north out of the SO get depleted of nutrients (DSi) by biologic (BSi) export to depth into southward moving water masses, thereby "trapping" DSi in the SO. By decelerating the cycling of DSi (e.g., by reducing the Si quota in sinking organic matter), the major trapping mechanism is weakened and the hypothesis is that this results in net DSi export, or leakage, out of the SO.

We define a measure of leakage or respective reduction in the "DSi trapping efficiency" as the ratio between oceanic inventory south of 40°S and the total global DSi inventory. Comparing *LGMfe* with *LGM*, we find a reduction of only 1%. This rather minute change is outweighed by the effect of the 36% reduction in DSi

demands, described above, which leads to a substantially damped biogeochemical DSi cycling and a reduction of BSi export to the sediments. The latter results in a global increase in the oceanic DSi content of 11%. Hence, even though the trapping efficiency in the SO is reduced, the SO does not lose DSi but rather gains ≈10% relative to simulation *LGM*. The increase in both local (in the SO) and global DSi concentrations triggers an overall decrease in δ^{30}Si of BSi (Figure 3b) which is generally roughly consistent with observations as far as the sign of changes in concerned.

3.3. LGMslack and LGMbreezy

The simulations *LGMslack* and *LGMbreezy* assume, in contrast to the reference simulation, that glacial winds differed from those today. Sign and magnitude of the change are controversially discussed in the literature. Here we test both a global halving *LGMslack* and a doubling *LGMbreezy* of wind speeds. The results are depicted in Figures 3c and 3d, with *LGMslack* featuring a generally higher δ^{30}Si of BSi in the SO, suggesting a straightforward underlying process: Reduced winds bring less DSi up to the sunlit surface which increases the effect of fractionating DSi uptake by algae in surface DSi (because there is less "flushing" of the system). As the substrate (surface DSi) becomes higher in δ^{30}Si, so does the associated BSi export.

In contrast, in *LGMbreezy* more DSi is upwelled in the SO. The effect of fractionation on the isotopic composition of the substrate is diluted by the additional DSi supply. As a consequence, δ^{30}Si of BSi mostly decreases and is consistent with observations in terms of the sign of simulated changes. But specifically in the SO, *LGMbreezy* features a sensitivity which is apparently too low.

Complexity is added to the rest of the ocean as the system adjusts: Enhanced (decreased) upwelling of nutrients by winds feed an increase (decrease) in export production which results in a global Si loss (gain) by increased (decreased) sedimentation such that the initial nutrient pulse is counteracted. Negative values, both in *LGMslack* and *LGMbreezy*, follow the overall patterns already discussed for *LGM*.

In summary, our model suggests that reduced winds are inconsistent with observed δ^{30}Si of BSi in the SO. In contrast, the effect of increasing winds appears to be more consistent with the observations of δ^{30}Si of BSi as far as the sign of changes is considered. In terms of magnitude, however, a doubling of the wind during the LGM fails to retrace most of the observations in the SO.

3.4. LGMtrickle and LGMflush

The experiments *LGMtrickle* and *LGMflush* assume that the supply of Si to the glacial ocean was different from today's. The default value (applied in all of our configurations except the two discussed here) for total supply of Si to the ocean (RRDSi) is 9.55 Tmol Si year^{-1} with an isotopic composition corresponding to 0.74‰ (RRδ^{30}; Table 1). The fractionating effect of marine biota increases the global mean δ^{30}Si of DSi relative to the supply because it preferentially exports BSi with lower δ^{30}Si to the sediment such that DSi with higher δ^{30}Si remains in the water column. From this we conclude that the larger (smaller) the supply in relation to the biotic turnover, the lower (higher) the δ^{30}Si in DSi—which ultimately controls the isotopic composition of BSi archived in sediments.

Figure 4 supports this conclusion: Panel (a) shows the difference between the simulation *LGMtrickle* and *PI*. Compared to Figure 3a, we find that the 20% reduction of Si supply to the ocean drives an overall increase in δ^{30}Si of BSi. Likewise, Figure 4b shows that a 20% increase in Si supply decreases the overall δ^{30}Si of BSi with the biggest effect concentrated in the eastern equatorial upwelling area.

In summary, the sensitivity of δ^{30}Si of BSi to changes in Si supply is too small to explain observed glacial interglacial variations. Expressed in terms of a global average of δ^{30}Si of BSi, we find less than 0.1‰ change when altering the Si supply by 40%.

3.5. LGMlight

Frings et al. (2016) suggest that the relatively low δ^{30}Si of BSi archived in glacial sediments are caused by a glacial isotopic composition of the Si supplied to the ocean that was 1‰ lighter than today. Consistent with their reasoning, we find in Figure 4c a global decrease in δ^{30}Si of BSi by up to 1‰ (with the eastern tropical Pacific being an exception) in response to the reduction of RRδ^{30}. Expressed in terms of a global oceanic average, we find a decrease of 0.65‰ at the end of our 10,000 year spinup.

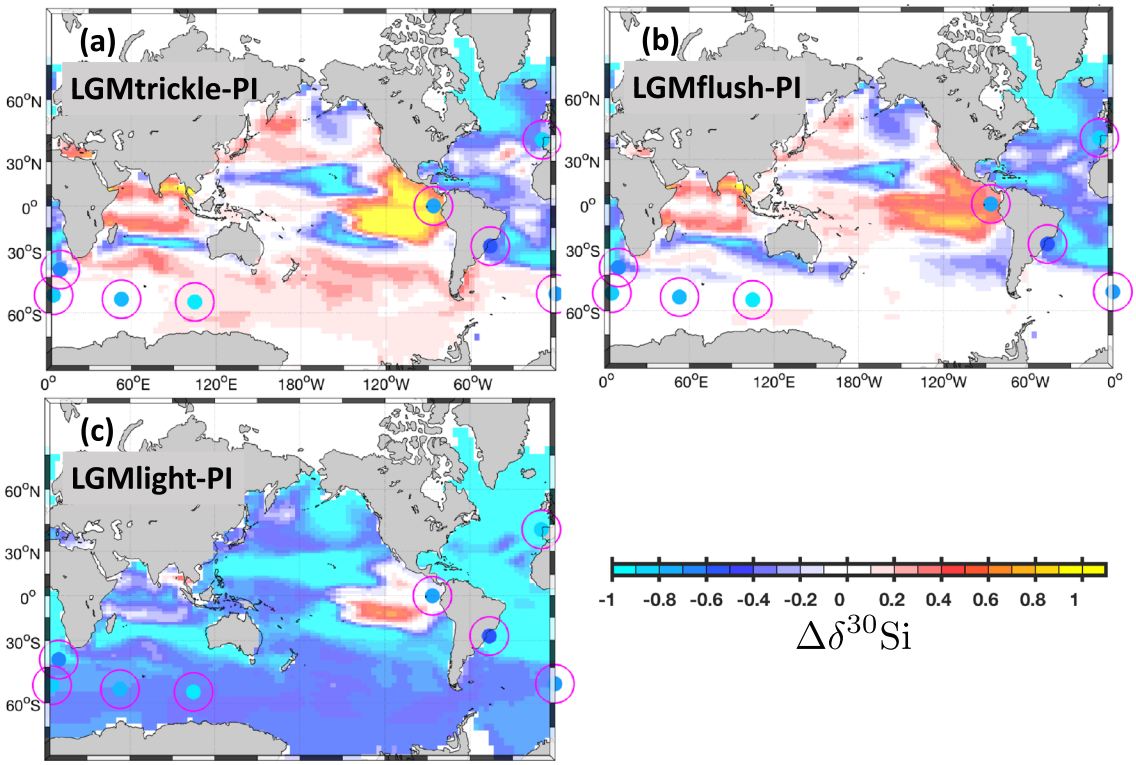

Figure 4. Difference in simulated δ^{30}Si of BSi relative to the preindustrial simulation *PI* as deposited to sediments in units of ‰. Panels (a)–(c) refer to differences *LGMtrickle-PI*, *LGMflush-PI*, and *LGMlight*, respectively. Magenta circles denote locations of observations of δ^{30}Si in BSi as preserved in sediment cores (see section 2.1).

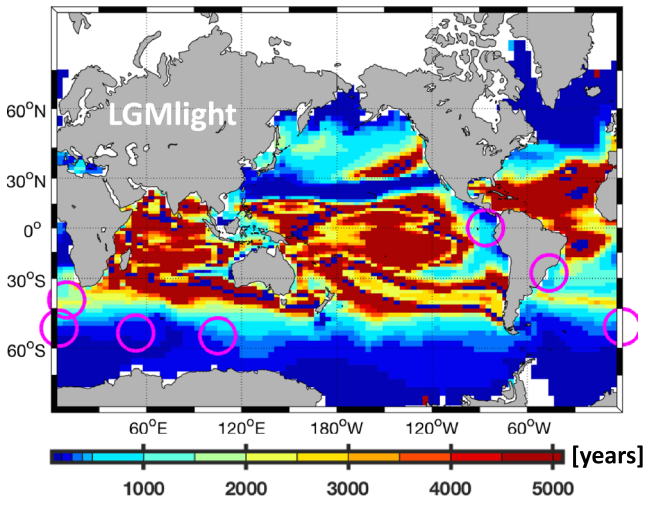

Figure 5. Timescale of manifestation of changes in δ^{30}Si of BSi archived in sediments simulated in *LGMlight* (as shown in Figure 3c) in units of years. White patches denote changes of less than 0.1‰ or regions with bottom BSi concentrations less than 10^{-10} mol Si m^3. Magenta circles denote locations of observations of δ^{30}Si in BSi as preserved in sediment cores (see section 2.1).

In summary, Figure 4c suggests that a reduction of δ^{30}Si in DSi supplied to the ocean drives changes that are consistent with almost all observations of glacial δ^{30}Si in BSi archived in sediments.

4. Discussion

In section 4.1 we discuss timescales at work, section 4.2 puts the results into perspective, and section 4.3 discusses potential and generic sources of uncertainties in the underlying Earth System Model.

4.1. Manifestation Timescales

So far, we explored the sensitivity of our model to changes in environmental conditions with numerical time slice experiments. This can be deceptive for, for example, processes that manifest themselves with timescales as long or longer than typical glacial interglacial cycles. In the following we use the concept of manifestation timescale introduced in section 2.3 in order to check if our simulated isotopic signatures of processes could possibly be detected in actual sediments—as opposed to being smeared out over one or more glacial interglacial cycles.

Figure 5 shows that manifestation timescales vary considerably over space. In terms of detectability, we find in *LGMlight* that manifestation timescales at the observational sites are short enough so that they should be detectable in sediments (if they were to have been at play). This suggests that the effect of changing isotopic composition of oceanic Si supply to the ocean would be clearly imprinted into the sediment record.

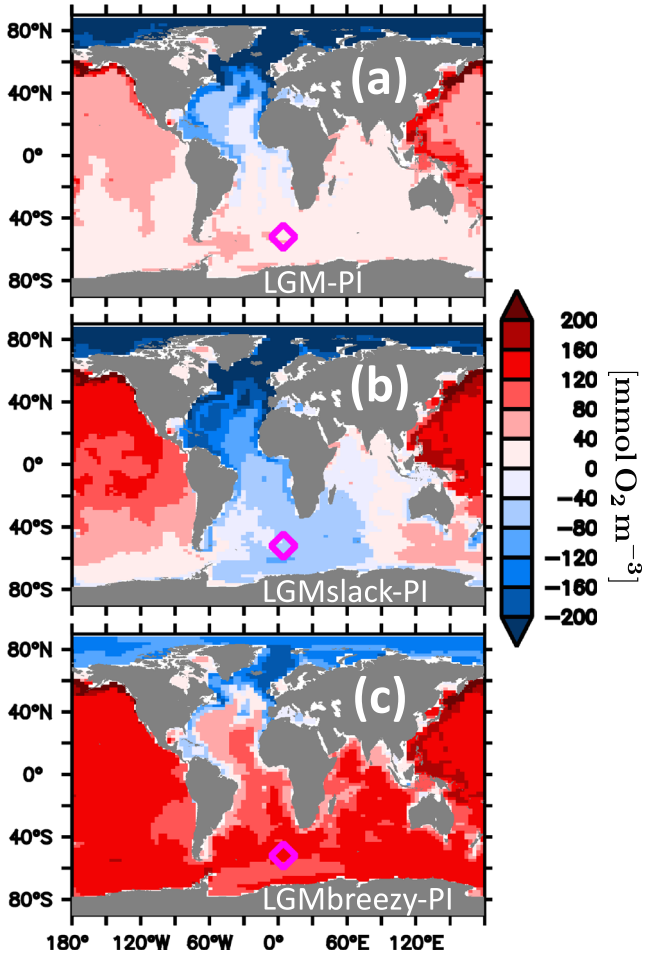

Figure 6. Simulated oxygen concentration at the bottom of the ocean relative to simulated preindustrial (PI) concentrations in units of mmol O_2 m^{-3}. Panels (a)–(c) refer to simulations *LGM, LGMslack*, and *LGMbreezy*, respectively.

This does not apply to *LGMbreezy* where manifestation timescales in the SO exceed 5,000 years (not shown).

4.2. Appraisal of Results

The two experiments *LGMbreezy* and *LGMlight*, out of our total of seven numerical sensitivity experiments, feature the best fit with respect to the sign to the overall, lower (relative to today) glacial δ^{30}Si of BSi observations. This holds especially in the SO. The experiment with increased winds (*LGMbreezy*), however, features a sensitivity which, although of correct sign, is much lower than suggested by observational evidence. In addition, *LGMbreezy* features very long manifestation timescales (when compared to *LGMlight*; cf., section 4.1) which implies that the process of increasing winds is, in reality, even harder to detect than the rather weak signal we find at the end of our 10,000 year-long numerical time slice experiment suggests. This leaves us with simulation *LGMlight* being the most consistent with observations of δ^{30}Si of BSi out of all considered processes (listed, e.g., in Table 2).

Even so, other processes such as changes to air-sea iron fluxes and wind fields may also have been at play. According to our model results, however, these should manifest themselves more prominently in metrics other than in the isotopic composition of BSi. One example of such a metric is sedimentary redox-sensitive trace-metal records. Jaccard et al. (2016) deduce from respective evidence glacially reduced dissolved oxygen concentrations in the Atlantic Sector of the deep SO. Figure 6 suggests that, in our model, a decrease in wind speeds does drive a consistent oxygen decrease, while unchanged winds, or an increase of winds, result in an inconsistent increase of simulated dissolved oxygen concentrations. Investigations of the link between decreasing winds and oxygen reveal two antagonistic processes being at work in our model. For one, the reduced wind-induced upwelling of nutrients drives less production and associated oxygen consumption in the SO. This, on its own, would increase the oxygen concentration. However, this process is opposed by a reduced wind-induced overturning which reduces ventilation and drives an oxygen decrease. The net effect differs among the sectors of the SO, such that the Atlantic Sector in Figure 6b is consistent with results from Jaccard et al. (2016). The difference among the sectors in the SO is facilitated by a reduced (down to 40% relative to *LGM*) Antarctic Circumpolar Current which reduces the zonal mixing between the sectors as a result of reduced winds supplying less momentum to the ocean. Please note that a comprehensive analysis of oceanic deoxygenation, which must cover the role of (preferably explicitly resolved) iron dynamics (see, e.g., Stoll, 2020) and more data (e.g., Jaccard & Galbraith, 2011), is beyond the scope of this manuscript which focuses on the isotopic composition of BSi in response to changing environmental conditions. Our main conclusion here is that *LGMbreezy* is apparently inconsistent with sedimentary redox-sensitive trace-metal records.

4.3. Model Uncertainties

Assessing the reliability of model projections is not straightforward. This applies to both climate models (Notz, 2015) and pelagic biogeochemical models (Löptien & Dietze, 2017). Our approach here is to highlight a choice of our simplifying ad hoc assumptions which may potentially degrade our model results:

- DSi supply by rivers. In our simulations, all DSi supplied from the land into the ocean is homogeneously distributed over the oceans. The rationale behind this is the sparse information available on glacial-interglacial changes in river loads and the implicit assumption that horizontal transports act on much shorter timescales than the vertical transports. Among the (unintended) consequences is a glacial Arctic Ocean which is continuously flushed by isotopically light DSi in our model—even though, in reality, it was covered by ice and probably did not receive any river runoff at all.

- Isotopic fractionation during BSi dissolution. In our setup this is not to account for—an approach we share with the pioneering three-dimensional modeling work of Wischmeyer et al. (2003), the box modeling work of Reynolds (2009), and the three-dimensional modeling work of Gao et al. (2016). Our simulation of deep δ^{30}Si of DSi (see Figure A7) fits into this successive model development in that it features a realistic gradient in the deep waters of the Atlantic and Pacific Oceans. In comparison, the early work of Wischmeyer et al. (2003) failed to simulate a significant gradient (less than 0.1‰ difference), while Reynolds (2009) and Gao et al. (2016) reported a more realistic difference of 0.3‰ between the basins. Our model features 0.5‰ which is even closer to the data-constrained model estimate of 0.7‰ by Holzer and Brzezinski (2016)—arguably the most comprehensive estimate of today's δ^{30}Si of DSi distribution in the deep ocean. Further comparison with the Holzer and Brzezinski (2016) estimate, however, reveals that our simulated variance in the deep Pacific is apparently too low: While results by Holzer and Brzezinski (2016) suggest a range between 1.7‰ in the South and 1.1‰ up North, we find barely any variation in our simulation *PI*. According to Holzer and Brzezinski (2016) and Beucher et al. (2008), this deficiency of our model is linked to not accounting for isotopic fractionation during BSi dissolution.
- Diagenetic DSi release from sediments. The results presented here are based on a setup which neglects DSi release from sediments—even though it is known to be a significant agent in the world ocean silica cycle (Tréguer & De La Rocha, 2013). This simplification was necessitated by the computational burden that is associated with the long timescales of sedimentary processes. In order to test for robustness of our results, however, we followed up on a suggestion that surfaced during the review process. As described in more detail in Appendix B1 we decreased the export of BSi out of the lowermost wet model grid box in order to mimic the effects of diagenetic DSi release from the sediments. In summary, the thereby modified model version which is more complex in the sense that it contains more tunable model parameters performed better in terms of simulated DSi concentrations. As concerns the misfit between simulated glacial interglacial δ^{30}Si of BSi differences, we find that our results as shown in Figure 3a are robust (when compared with Figure B2).
- Variable Si isotopic fractionation by diatoms. We apply the constant fractionation factor $\alpha_1 = 0.9989$ (De La Rocha et al., 1997; Gao et al., 2016) even though contradictory evidence suggests that fractionation factors vary among species (Sutton et al., 2013) and that Fe availability may modulate fractionation (Cavagna et al., 2011; Meyerink et al., 2017).

A problematic region where our model simulations deviate substantially from observations of δ^{30}Si of BSi is the eastern equatorial Pacific in Figures 3 and 4. We speculate that this is associated with an unrealistic zonal circulation in our model which is apparently endemic to the current generation of coupled ocean circulation biogeochemical models (Dietze & Löptien, 2013; Getzlaff & Dietze, 2013).

In summary, we refer to a model that is capable of reproducing the effects of the (preindustrial) circulation and isotopic fractionation during BSi production with a fidelity comparable to existing non-data-assimilated three-dimensional coupled ocean circulation biogeochemical models. Compared with the arguably most comprehensive data-assimilated model estimate of the present abyssal δ^{30} of DSi, we miss an intra-basin variability in the Pacific Ocean that is probably linked to unaccounted isotopic fractionation during BSi dissolution.

5. Conclusions

We set out to simulate δ^{30}Si of BSi (such as opal) archived in oceanic sediments under modern climates (PI) and glacial conditions (LGM). Specifically, we implement and test several hypotheses which were suggested in the literature to explain the observed difference in δ^{30}Si of BSi between PI and LGM.

Our numerical experiments with an EMIC suggest that neither of the following processes effected glacial-interglacial changes in the isotopic composition of BSi is consistent with observations: (1) an overall cooling and substantial reduction of the MOC (our experiment *LGM*), (2) a decrease of Si:N quota in diatoms as potentially effected by increased air-sea iron fluxes (our experiment *LGMfe*), (3) decreasing winds (our experiment *LGMslack*), and (4) increasing or decreasing Si supply to the ocean (our experiments *LGMtrickle* and *LGMflush*).

Out of seven sensitivity experiments, only the simulation with increased winds (experiment *LGMbreezy*) and the simulation with a changed isotopic composition of river runoff (experiment *LGMlight*) reproduce the

observed sign of change, specifically in the SO. The experiment with increasing winds (experiment *LGMbreezy*), however, fails to reproduce the magnitude of observed changes and is, furthermore, inconsistent with the Jaccard et al. (2016) estimate of dissolved near-bottom oxygen concentrations (based on redox-sensitive trace-metal records archived in the sediments in the Atlantic Sector of the SO). The experiment *LGMlight* is most consistent with observed changes in δ^{30}Si of BSi in terms of both sign and magnitude. This confirms the suggestions by Frings et al. (2016) that changes in the isotopic composition of DSi supplied to the ocean (rather than changes in the internal oceanic cycling of DSi) triggered low glacial δ^{30}Si of BSi. Further, the estimated manifestation timescale of changes in δ^{30}Si of BSi ranges between several hundreds to 2,500 years at the observational sites. This means that the respective signal should be detectable—despite a global turnover timescale of DSi, which is comparable to the period of glacial-interglacial cycles.

As a side aspect, we find a simulated oceanic DSi inventory which is 10–20% lower during the Last Glacial Maximum than today. This is somewhat counterintuitive because simulated BSi production is also lower during the LGM which suggests that less BSi is sinking down to the oceanic sediment. More comprehensive analysis shows that this effect is outweighed by BSi dissolution rates that are also slowed down as a consequence of colder temperatures such that more BSi escapes dissolution prior to sedimentation in our model.

Caveats remain. A major problem of developing a Si module within the framework of an Earth System Model is the high computational cost associated with running test simulations to equilibrium. To this end, a turnover timescale of Si in the ocean of more than 10,000 years is a real handicap. Among the simplifications we chose in order to limit the number of test simulations was discarding the effect of fractionation during BSi dissolution. According to Holzer and Brzezinski (2016) and Beucher et al. (2008), this may be the reason why our model does not reproduce observed variations of δ^{30}Si of DSi within the Pacific. Further—substantial—uncertainty is added by the generic problem of constraining global biogeochemical ocean models (Löptien & Dietze, 2015, 2017, 2019).

Appendix A: Model Assessment

The UVic ESCM reference version we use for *LGM* and *PI* has been described and assessed by Brennan et al. (2012). We left this base module unchanged. In the following we refer to our extension adding a Si cycle (which does not feedback onto the original modules) in the following.

Figure A1 shows the modern climate (PI) simulated DSi concentrations at the surface and at depth compared to observations (Garcia, Locarnini, Boyer, & Antonov, 2010). A comparison of panels (a) and (c)

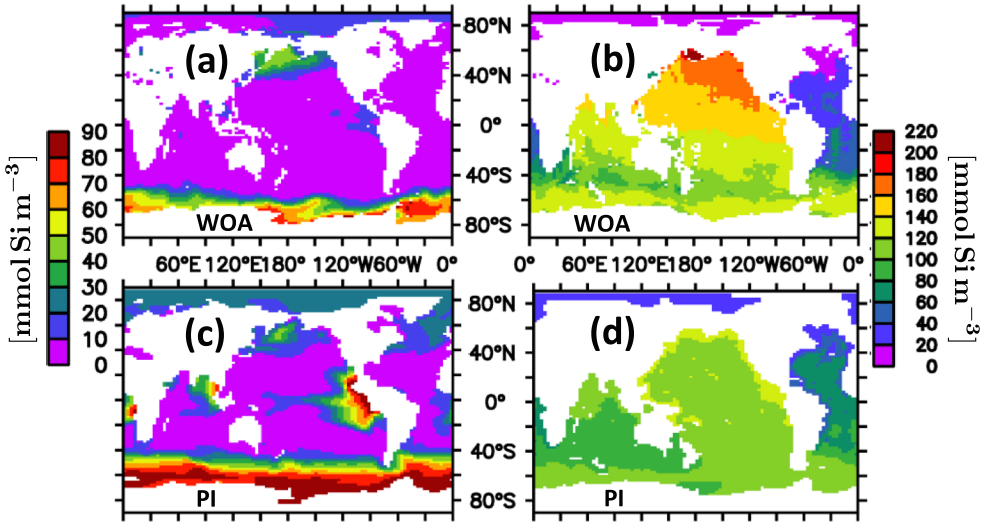

Figure A1. Surface and deep (2,000 m to bottom average) DSi concentrations in units of mmol Si/m^3. Panels (a) and (b) refer to surface and abyssal observations (Garcia, Locarnini, Boyer, & Antonov, 2010), respectively. Panels (c) and (d) refer to simulated preindustrial (*PI*) surface and abyssal concentrations, respectively.

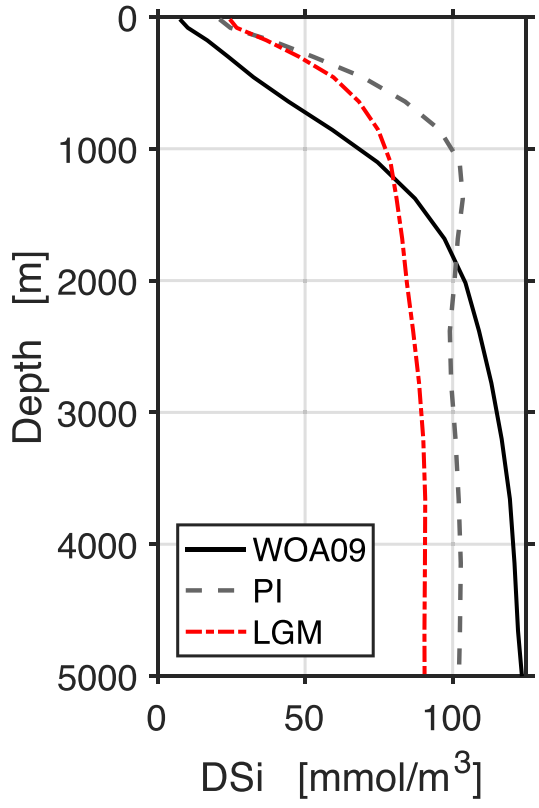

Figure A2. Zonally and meridionally averaged vertical profile of DSi concentrations in units of mmol Si m^3. The black, gray dashed, and red dash-dotted lines refer to observations (black line; Garcia, Locarnini, Boyer, & Antonov, 2010), preindustrial simulation, and Last Glacial Maximum simulation, respectively.

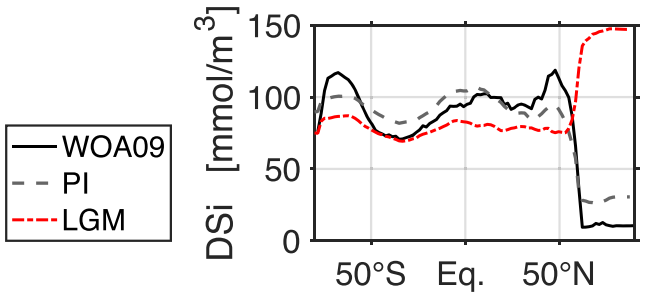

Figure A3. Zonally and vertically averaged DSi concentrations in units of mmol Si m^{-3}. The black, gray dashed, and red dash-dotted lines refer to observations (black line; Garcia, Locarnini, Boyer, & Antonov, 2010), preindustrial simulation, and Last Glacial Maximum simulation, respectively.

suggests that the simulated DSi concentrations are somewhat too high at the surface, specifically in the tropics and the southern part of the SO. At the same time, DSi concentrations are too low at the bottom, specifically in the northern Pacific (panels [b] and [d]). These deviations are also visible in the global mean profiles in Figure A2.

We suspect that these differences are both the result of our choice of parameters (possibly an underestimated opal sinking velocity and an underestimated molecular DSi to phosphate stoichiometric ratio or an underestimated BSi production rate) and being caused by rather coarse spatial resolution of the ocean module which is known to retard ocean transports (e.g., Getzlaff & Dietze, 2013). An additional cause for model data misfits of DSi concentrations is followed up in Appendix B1 where we added a brief investigation into the effect of diagentic DSi release from sediments.

Figure A3 depicts zonally and vertically averaged DSi concentrations. While the above-mentioned biases map also onto this metric, the major features are, nevertheless, captured. Specifically, the trapping of DSi in the SO, high values in the tropics, and a large drop in the Arctic are clearly visible. Not well captured are, however, the midlatitudes in the Northern Hemisphere where the simulated concentrations are underestimated. Further, the transition zone to the SO is not as sharp as observed and DSi values in the Arctic are somewhat overestimated.

Figures A4 and A5 show meridional sections of both simulated DSi and phosphate in comparison to the observations. This allows for a continuative exploration of the reasons for model-data mismatches with respect to DSI: The section through the Atlantic (at 30°W) shows simulated DSi concentrations that are generally underestimated, while phosphate seems in better agreement with the observations in that respect. In the SO, however, both variables are biased—and the biases oppose one another: In terms of SO nutrient trapping, simulated phosphate is trapped more efficiently than indicated by the observations. This is mirrored by the low bias of simulated SO dissolved oxygen concentrations (Figure A6) indicating an overestimation of accumulated remineralization. This is in contrast to simulated DSi concentrations, where the simulated SO nutrient trapping is too weak. With one nutrient biased high and the other nutrient biased low, it seems unlikely that a deficient circulation is the cause for these biases (although this cannot be ruled out). Hence, the SO nutrient trapping apparently relates strongly to the biogeochemical model parameters. One conclusion from this may be that the biogeochemical model is better tuned with respect to phosphate than to DSi. This is to be expected because of the wider use of the phosphate-based biogeochemical model and the much shorter equilibration timescales for phosphate which facilitate the respective tuning to observations. In the Pacific, however, the situation differs, and subsurface maxima in the Northern Hemisphere (except the Arctic) are too low for both phosphate and DSi. Following our reasoning above, this may be indicative for flaws in the ocean circulation module. Please note, however, that the attribution of flaws in model behavior to respective processes is challenging and may even be impossible given the current set of observations (e.g., Löptien & Dietze, 2019).

Table A1 provides a quantitative estimate of how our DSi/BSi module compares against the underlying biogeochemical and ocean circulation

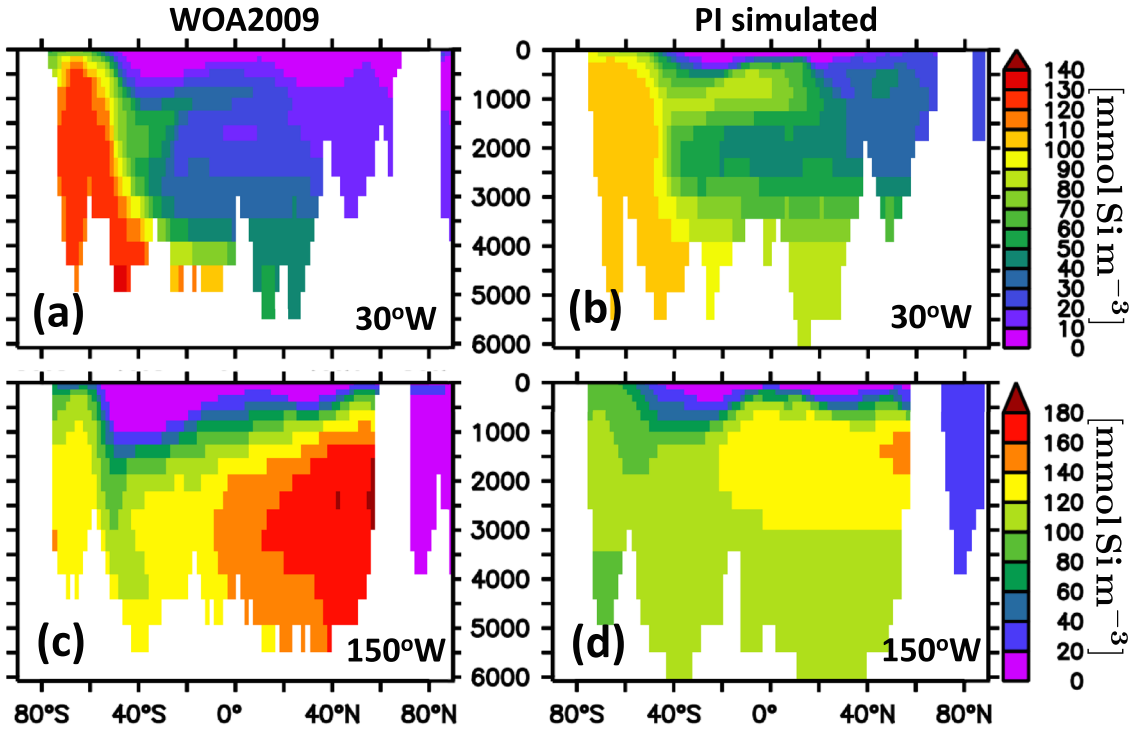

Figure A4. Meridional sections over depth (m) of DSi in units of mmol Si m^{-3}. Panels (a) and (c) refer to observations (Garcia, Locarnini, Boyer, & Antonov, 2010) and panels (b) and (d) to the preindustrial simulation.

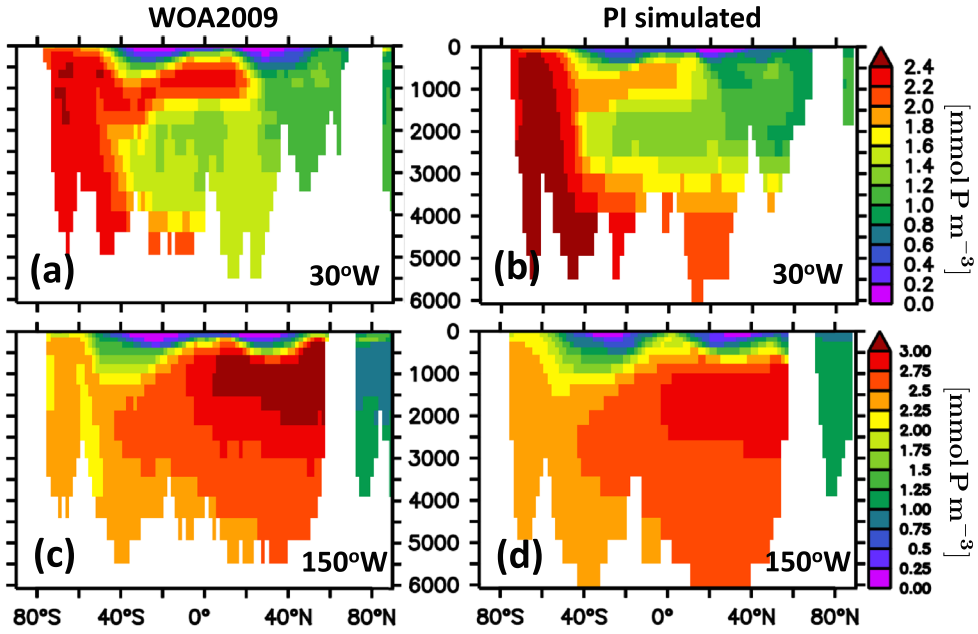

Figure A5. Meridional sections over depth (m) of PO_4 in units of mmol P m^{-3}. Panels (a) and (c) refer to observations (Garcia, Locarnini, Boyer, & Antonov, 2010) and panels (b) and (d) to the preindustrial simulation.

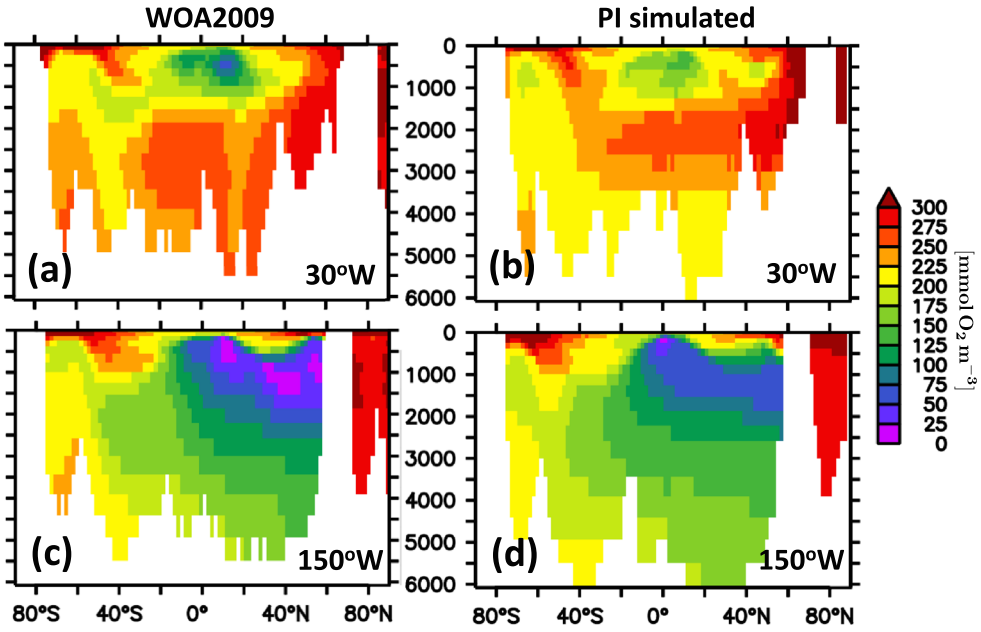

Figure A6. Meridional sections over depth (m) of dissolved O_2 in units of mmol O_2 m^{-3}. Panels (a) and (c) refer to observations (Garcia, Locarnini, Boyer, Antonov, et al., 2010) and panels (b) and (d) to the preindustrial simulation.

module of Brennan et al. (2012). The simulated temperature variance is overestimated by 3% and the temperature bias is 0.6 K, corresponding to 9% relative to the standard deviation in the observations. The respective bias to standard deviation of salinity is with 0.03 even smaller (5% relative to the standard deviation in the observations). Simulated phosphate concentrations are, surprisingly, even closer to observations than simulated salinities (note that this does also apply to simulated dissolved oxygen concentrations): The bias to standard deviation ratio is smaller (4%) and the simulated variance covers 86% of observed levels (versus 70% for salinity). Given that the salinity distribution directly affects ocean circulation via density driven pressure gradients, it is remarkable that the misfit in this active physical property can be much larger than the misfit of the rather passive (in terms of their effect on circulation) phosphate whose distribution is directly shaped by oceanic circulation. This may be an indication that the biogeochemical module of Brennan et al. (2012) has been "overly successfully" tuned to a flawed physics (a process illustrated by Löptien & Dietze, 2019). In contrast, the simulated DSi features the largest deviations among the metrics reviewed here. The simulation features a variance corresponding to 54% of observed levels, and the simulated bias is 21% relative to the observed standard deviation. The correlation of simulated DSi concentrations with observations is, however, rather good in the sense that it is very similar to that of salinity (0.84 versus 0.85).

Table A1
Comparison Between Observations (OBS) and Preindustrial Simulation (PI)

Variable	Unit	Std. OBS	Std. *PI*	Bias (*PI*-OBS)	RMS	Corr. coeff.	Var(*PIref*)/ var(OBS)
Temp.	*°C*	6.5	6.6	0.6	1.4	0.98	103%
Sal.	*PSU*	0.6	0.5	0.03	0.3	0.85	70%
PO_4	mmol P m^{-3}	0.83	0.77	−0.03	0.3	0.94	86%
O_2	mmol O_2 m^{-3}	77	75	2	28	0.93	95%
DSi	mmol Si m^{-3}	54	40	11	30	0.84	54%
$\delta^{30}DSi$	‰	0.62	0.48	0.57	0.56	0.51	60%

Note. Temp., Sal., std., RMS, corr. coeff., and var refer to temperature, salinity, standard deviation, root-mean-square error and correlation coefficient between PI and OBS, and variance, respectively. $\delta^{30}DSi$ refers to surface values. The origin of observations is documented in section 2.1.

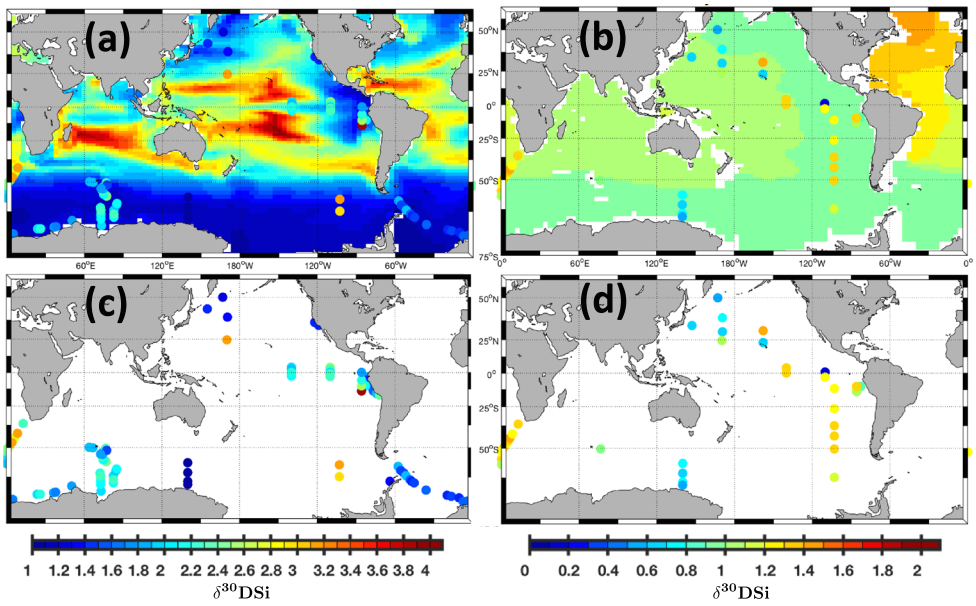

Figure A7. δ^{30} DSi at the surface (50 m, panels [a] and [c]) and at depth (2,000 m, panels [b] and [d]) in units of ‰. The colored blobs denote those observations (see section 2.1) within 0–100 m (1,500–2,500 m) that are closest to the nominal depth of 50 m (2,000 m). The background color in panels (a) and (b) refers to simulation PI. Panels (c) and (d) show respective observations only to facilitate their recognition.

Figure A7 shows our simulated preindustrial δ^{30}DSi distribution. The sparseness of observational data with often times puzzling inhomogeneities illustrates the Hendry and Brzezinski (2014) conclusion that the δ^{30}DSi data set is "...inadequate to evaluate mechanisms leading to even the first-order distribution of isotopes of Si in the global ocean." Also, we are urged to compare point observations to large-scale averages, resolved by the model. The relatively low correlation of 0.51 between model and observations has thus to be considered with some caution. Please note that a clearer picture seems to be found for the more abrupt events of the deglacial, leading to the Silicic Acid Ventilation Hypothesis of Hendry and Brzezinski (2014).

Appendix B: Silica Dissolution Rates, Temperature, and Diagenetic DSi Release From Sediments

One of the major processes at work in our simulations is a reduced glacial oceanic DSi inventory (relative to preindustrial). Lower glacial temperatures slow down BSi dissolution such that more BSi sinks into the sediments where it is lost forever in our model. In turn, the overall reduced availability of DSi invokes more DSi limitation which manifests itself in a glacial tendency toward higher δ^{30}DSi which is apparently inconsistent with the observed tendency to generally lower glacial δ^{30}DSi.

During the review process of an earlier version of this manuscript, the following concerns were put forward: Our model does not account for diagenetic release of DSi from sediments even though it is known to be substantial (e.g., Tréguer & De La Rocha, 2013). Hence, our model neglects a process that retains Si in the ocean.

Table B1
Comparison Between Observations (OBS) and Preindustrial Simulation (PI)*

Variable	Unit	Std. OBS	Std. *PI*	Bias (*PI*-OBS)	RMS	Corr coeff.	var(*PIref*)/ var(OBS)
DSi	mmol Si m^{-3}	54	49	−1.2	15	0.96	83%
δ^{30}*DSi*	‰	0.62	0.60	−0.29	0.58	0.54	93%

Note. std., RMS, corr. coeff., var refer to standard deviation, root-mean-square error between simulation *PI** and OBS, and variance, respectively. δ^{30}*DSi* refers to surface values. The origin of observations is documented in section 2.1.

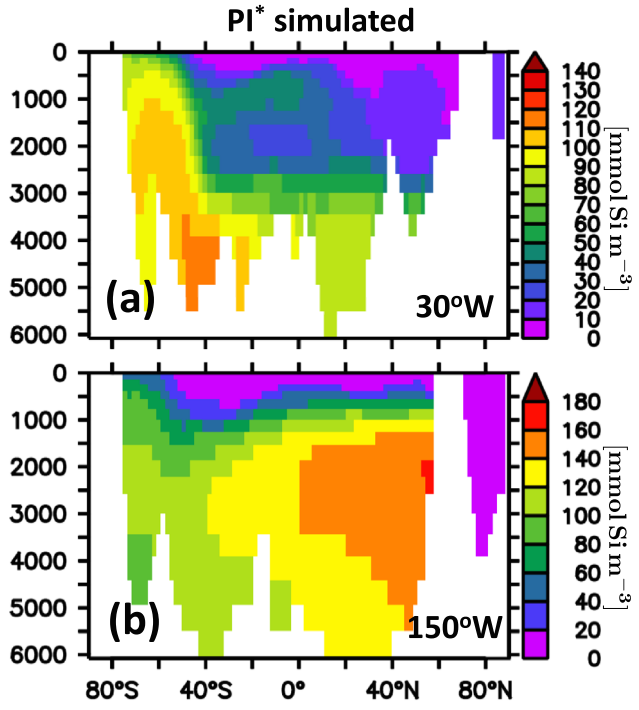

Figure B1. Meridional sections over depth (m) of DSi in units of mmol Si m^{-3}. Panels (a) and (b) refer to simulation PI^* that applies the Gao et al. (2016) opal dissolution rate $A = 333^{-1}$ day^{-1} and that mimics diagenetic release of DSi from sediments by reducing the sinking velocity of BSi from 10 to 0.5 m day^{-1} in the lowermost wet model grid box.

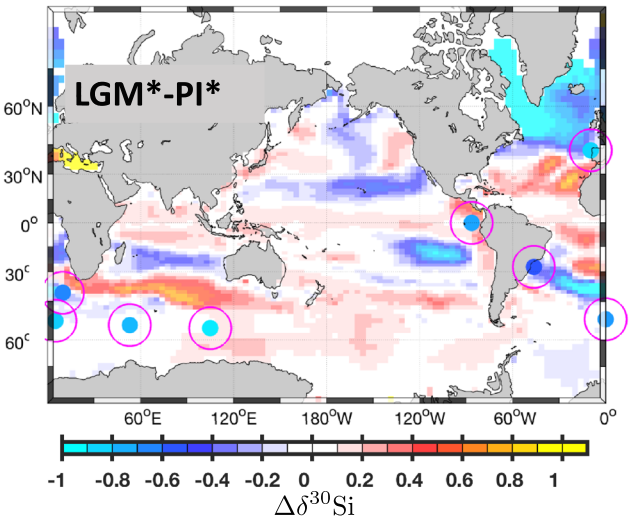

Figure B2. Difference in simulated LGM δ^{30}Si of BSi relative to the preindustrial simulation PI^* as deposited to sediments in units of ‰. The difference to Figure 3a is that both LGM^* and PI^* refer to simulations that apply the Gao et al. (2016) opal dissolution rate $A = 333^{-1}$ day^{-1} and that mimic diagenetic release of DSi from sediments by reducing the sinking velocity of BSi from 10 to 0.5 m day^{-1} in the lowermost wet model grid box.

Even so, our simulated DSi inventory is close to observations—because we adjusted the silica dissolution rate accordingly (Figure 1). This procedure yielded a functional dependency of silica dissolution and temperature which is at the lower end of data compiled by Kamatani (1992) and shown in Figure 2. In the following we will discuss if this may have flawed our results.

We integrate an additional set of model simulations dubbed PI^* and LGM^* for 10,000 years (starting from the spun up simulations *PI* and *LGM*). PI^* and LGM^* are identical to *PI* and *LGM* except for the following: (1) We use the Gao et al. (2016) opal dissolution rate $A = 333^{-1}$ day^{-1} which yields a functional dependency of silica dissolution and temperature which is at the upper end of data compiled by Kamatani (1992) and shown in Figure 2. (2) We reduce the sinking velocity of BSi out of the lowermost wet model grid box from 10 down to 0.5 m day^{-1} in order to mimic the effect of diagenetic DSi release (or, more specifically, the increased residence time of Si at the bottom of the water column).

Integration of PI^* for 10,000 years resulted in a fairly equilibrated DSi inventory close to observations (≈3% less than Garcia, Locarnini, Boyer, & Antonov, 2010). The DSi concentrations of PI^* are more realistic than in the reference version *PI*. In terms of root-mean-square error the misfit drops substantially from 30 (Table A1) down to 15 mmol Si m^{-3} (Table B1). The increase in realism is confirmed by visually inspecting Figure B1 versus Figure A4.

In terms of $\delta^{30}DSi$ we find that PI^* features a variance more similar to observations compared to *PI* (93% versus 60%; Table B1 versus Table A1). The correlation does, however, not improve—probably because we do not account for isotopic fractionation during BSi dissolution (see discussion in section 4.3).

In summary, PI^* features a more realistic DSi distribution, more realistic levels of $\delta^{30}DSi$ variance, and a (rough) representation of diagenetic DSi release from the sediments. Further, PI^* features a functional dependency of silica dissolution and temperature that is at the upper end of data compiled by Kamatani (1992)—as opposed to *PI* which features a functional dependency that is at the lower end. Even so, the glacial-interglacial sensitivity of δ^{30}Si of BSi is apparently robust: Figure B2 shows the LGM^*–PI^* difference that is similar to the respective *LGM - PI* difference in Figure 3a in that the simulated changes are opposing the observational evidence.

Data Availability Statement

Data are available through Locarnini et al. (2010); Antonov et al. (2010); Garcia, Locarnini, Boyer, and Antonov, 2010; Garcia, Locarnini, Boyer, Antonov, et al., 2010; Beucher et al. (2008); Cardinal et al. (2005); De La Rocha et al. (2011); de Souza, Reynolds, Johnson, et al., (2012); de Souza, Reynolds, Rickli, et al., (2012); Ehlert et al. (2012); Fripiat, Cavagna, Dehairs, et al., (2011); Fripiat, Cavagnam, Savoye, et al., 2011; Grasse et al. (2013); Reynolds et al. (2006); Frings et al. (2016); Brzezinski et al. (2002); De La Rocha et al. (2011, 1997, 1998); Ehlert et al. (2013); Ellwood et al. (2010); Hendry et al (2012, 2016); Horn et al. (2011); and Pichevin et al. (2009). The model configurations and output are archived online (https://zenodo.org/record/3959258#.XxsN6B1CRTY under doi:10.5281/zenodo.3959257).

Acknowledgments

H. D. and U. L. acknowledge funding by Deutsche Forschungsgemeinschaft (DFG) in the framework of the priority program *Antarctic Research with comparative investigations in Arctic ice areas SPP 1158* by Grant *SCHN 762/5-1*. We acknowledge discussions with Mark Holzer and Katrin Meissner. Katrin Meissner provided the model configuration (to which we added the Si cycle) by sharing code and forcing files. Fruitful discussion with Richard Matear and Andrew Lenton were made possible by DFG Grants *DI 1665/6-1* and *LO 1377/5-1*. A number of very good review papers eased the entry of H. D. and U. L. into the field. We are grateful to each and everyone sharing observational data. We thank one anonymous reviewer, Christoph Voelker, and the editorial team for their constructive work and effort! Open access funding enabled and organized by Projekt DEAL.

References

Antonov, J. I., Seidov, D., Boyer, T. P., Locarnini, R. A., Mishonov, A. V., Garcia, H. E., et al. (2010). World ocean atlas 2009, volume 2 salinity. *NOAA atlas NESDIS 69* (pp. 184). Washington, DC.: U.S. Government Priniting Office.

Bauer, P., Thorpe, A., & Brunet, G. (2015). The quiet revolution of numerical weather prediction. *Nature*, *525*(7567), 47–55. https://doi.org/10.1038/nature14956

Beucher, C. P., Brzezinski, M. A., & Jones, J. L. (2008). Sources and biological fractionation of silicon isotopes in the Eastern Equatorial Pacific. *Geochimica et Cosmochimica Acta*, *72*, 3063–3073. https://doi.org/10.1016/j.gca.2008.04.021

Beucher, C. P., Brzezinski, M. A., & Jones, J. L. (2011). Mechanisms controlling silicon isotope distribution in the Eastern Equatorial Pacific. *Geochimica et Cosmochimica Acta*, *75*, 4286–4294. https://doi.org/10.1016/j.gca.2011.05.024

Braconnot, P., Harrison, S. P., Kageyama, M., Bartlein, P. J., Masson-Delmotte, V., Abe-Ouchi, A., et al. (2012). Evaluation of climate models using palaeoclimatic data. *Nature Climate Change*, *2*, 417–424. https://doi.org/10.1038/NCLIMATE1456

Brennan, C. E., Weaver, A. J., Eby, M., & Meissner, K. J. (2012). Modelling oxygen isotopes in the university of Victoria Earth System Climate Model for preindustrial and last glacial maximum conditions. *Atmosphere-Ocean*, *50*(4), 447–465. https://doi.org/10.1080/07055900.2012.707611

Brzezinski, M. A., Pride, C. J., Franck, V. M., Sigman, D. M., Sarmiento, J. L., Matsumoto, K., et al. (2002). A switch from $Si(OH)_4$ to NO_3^- depletion in the glacial Southern Ocean. *Geophysical Reserach Letters*, *29*(12), 1564. https://doi.org/10.1029/2001GL014349

Cardinal, D., Alleman, L. Y., Dehairs, F., Savoye, N., Trull, T. W., & André, L. (2005). Relevance of silicon isotopes to Si-nutrient utilization and Si-source assessment in Antarctic waters. *Global Biogeochemical Cycles*, *19*, GB2007. https://doi.org/10.1029/2004GB002364

Cavagna, A.-J., Fripiat, F., Dehairs, F., Wolf-Gladrow, D., Cisewski, B., Savoye, N., et al. (2011). Silicon uptake and supply during a Southern Ocean iron fertilization experiment (EIFEX) tracked by Si isotopes. *Limnology and Oceanography*, *56*(1), 147–160. https://doi.org/10.4319/lo.2011.56.1.0147

Closset, I., Cardinal, D., Rembauville, M., Thil, F., & Blain, S. (2016). Unveiling the Si cycle using isotopes in an iron-fertilized zone of the Southern Ocean: from mixed-layer supply to export. *Biogeosciences*, *13*, 6049–6066. https://doi.org/10.5194/bg-13-6049-2016

Coplen, T. B., Hopple, J. A., Böhlke, J. K., Peiser, H. S., Rieder, S. E., Krouse, H. R., et al. (2002). Compilation of minimum and maximum isotope ratios of selected elements in naturally occurring terrestrial materials and reagents (*Water-Resources Investigation Report, 01-4222*). Reston Virginia: U.S Department of the Interior and 2, Geological Survey.

De La Rocha, C. L., Bescont, P., Croguennoc, A., & Ponzevera, E. (2011). The silicon isotopic composition of surface waters in the Atlantic and Indian sectors of the Southern Ocean. *Geochimica et Cosmochimica Acta*, *75*, 5283–5295. https://doi.org/10.1016/j.gca.2011.06.028

De La Rocha, C. L., Brzezinski, M. A., & De Niro, M. J. (1997). Fractionation of silicon isotopes by marine diatoms during biogenic silica formation. *Geochimica et Cosmochimica Acta*, *61*(23), 5051–5056. https://doi.org/10.1016/S0016-7037(97)00300-1

De La Rocha, C. L., Brzezinski, M. A., De Niro, M. J., & Shemesh, A. (1998). Silicon-isotope composition of diatoms as an indicator of past oceanic change. *Nature*, *395*, 680–683. https://doi.org/10.1038/27174

de Souza, G. F., Reynolds, B. C., Johnson, G. C., Bullister, J. L., & Bourdon, B. (2012). Silicon stable isotope distribution traces Southern Ocean export of Si to the South Pacific thermocline. *Biogeosciences*, *9*, 4199–4213. https://doi.org/10.5194/bg-9-4199-2012

de Souza, G. F., Reynolds, B. C., Rickli, J., Frank, M., Saito, M. A., Gerringa, L. J. A., & Bourdon, B. (2012). Southern Ocean control of silicon stable isotope distribution in the deep Atlantic Ocean. *Global Biogeochemical Cycles*, *26*, GB2035. https://doi.org/10.1029/2011GB004141

Dietze, H., & Löptien, U. (2013). Revisiting "nutrient trapping" in global coupled biogeochemical ocean circulation models. *Global Biogeochemical Cycles*, *27*, 265–284. https://doi.org/10.1002/gbc.20029

Ehlert, C., Grasse, P., & Frank, M. (2013). Changes in silicate utilisation and upwelling intensity off Peru since the Last Glacial Maximum—Insights from silicon and neodymium isotopes. *Quaternary Science Reviews*, *72*, 18–35. https://doi.org/10.1016/j.quascirev.2013.04.013

Ehlert, C., Grasse, P., Mollier-Vogel, E., Böschen, T., Franz, J., de Souza, G. F., et al. (2012). Factors controlling the silicon isotope distribution in waters and surface sediments of the Peruvian coastal upwelling. *Geochimica et Cosmochimica Acta*, *99*, 128–145. https://doi.org/10.1016/j.gca.2012.09.038

Ellwood, M. J., Wille, M., & Maher, W. (2010). Glacial silicic acid concentration in the Southern Ocean. *Science*, *330*(6007), 1088–1091. https://doi.org/10.1126/science.1194614

Franck, V. M., Brzezinski, M. A., Coale, K. H., & Nelson, D. M. (2000). Iron and silicic acid concentrations regulate Si uptake north and south of the Polar Frontal Zone in the Pacific Sector of the Southern Ocean. *Deep-Sea Research Part II*, *47*, 3315–3338. https://doi.org/10.1016/S0967-0645(00)00070-9

Frings, P. J., Clymans, W., Fontorbe, G., De La Roche, C. L., & Conley, D. J. (2016). The continental Si cycle and its impact on the ocean Si isotope budget. *Chemical Geology*, *425*, 12–36. https://doi.org/10.1016/j.chemgeo.2016.01.020

Fripiat, F., Cavagna, A.-J., Dehairs, F., de Brauwere, A., André, L., & Cardinal, D. (2012). Processes controlling the Si-isotopic composition in the Southern Ocean and application for paleoceanography. *Biogeosciences*, *9*, 2443–2457. https://doi.org/10.5194/bg-9-2443-2012

Fripiat, F., Cavagna, A.-J., Dehairs, F., Speich, S., André, L., & Cardinal, D. (2011). Silicon pool dynamics and biogenic silica export in the Southern Ocean inferred from Si-isotopes. *Ocean Science*, *7*, 533–547. https://doi.org/10.5194/os-7-533-2011

Fripiat, F., Cavagnam, A.-J., Savoye, N., Dehairs, F., André, L., & Cardinal, D. (2011). Isotopic constraints on the Si-biogeochemical cycle of the Antarctic Zone in the Kerguelen area (KEOPS). *Marine Chemistry*, *123*, 11–22. https://doi.org/10.1016/j.marchem.2010.08.005

Gao, S., Wolf-Gladrow, D. A., & Völker, C. (2016). Simulating the modern δ^{30}si distribution in the oceans and in marine sediments. *Global Biogeochemical Cycles*, *30*, 120–133. https://doi.org/10.1002/2015GB005189

Garcia, H. E., Locarnini, R. A., Boyer, T. P., & Antonov, J. I. (2010). World ocean atlas 2009, volume 4: Nutrients (phosphate, nitrate, silicate). In S. Levitus (Ed.), *NOAA atlas NESDIS 71* (pp. 398). Washington, DC.: U.S. Government Printing Office.

Garcia, H. E., Locarnini, R. A., Boyer, T. P., Antonov, J. I., Baranova, O. K., Zweng, M. M., & Johnson, D. R. (2010). World ocean atlas 2009, volume 3: Dissolved oxygen. In S. Levitus (Ed.), *Apparent oxygen utilization, and oxygen saturation* (pp. 344). Washington, D.C.

Georg, R. B., West, A. J., Basu, A. R., & Halliday, A. N. (2009). Silicon fluxes and isotope composition of direct groundwater discharge into the Bay of Bengal and the effect on the global ocean silicon isotope budget. *Earth and Planetary Science Letters*, *283*, 67–74. https://doi.org/10.1016/j.epsl.2009.03.041

Getzlaff, J., & Dietze, H. (2013). Effects of increased isopycnal diffusivity mimicking the unresolved equatorial intermediate current system in an earth system climate model. *Geophysical Research Letters*, *40*, 10. https://doi.org/10.1002/grl.50419

Grasse, P., Ehlert, C., & Frank, M. (2013). The influence of water mass mixing on the dissolved Si isotope composition in the Eastern Equatorial Pacific. *Earth and Planetary Science Letters*, *380*, 60–71. https://doi.org/10.1016/j.epsl.2013.07.033

Hawkins, J. R., Hatton, J. E., Hendry, K. R., de Souza, G. F., Wadham, J. L., Ivanovic, R., et al. (2018). The silicon cycle impacted by past ice sheets. *Nature Communicationa*, *9*, 3210. https://doi.org/10.1038/s41467-018-05689-1

Hendry, K. R., & Brzezinski, M. A. (2014). Using silicon isotopes to understand the role of the Southern Ocean in modern and ancient biogeochemistry and climate. *Quaternary Science Reviews*, *89*, 13–26. https://doi.org/10.1016/j.quascirev.2014.01.019

Hendry, K. R., Gong, X., Knorr, G., Pike, J., & Hall, I. R. (2016). Deglacial diatom production in the tropical North Atlantic driven by enhanced silicic acid supply. *Earth and Planetary Science Letters*, *438*, 122–129. https://doi.org/10.1016/j.epsl.2016.01.016

Hendry, K. R., Robinson, L. F., Meredith, M. P., Mulitza, S., Chiessi, C. M., & Arz, H. (2012). Abrupt changes in high-latitude nutrient supply to the Atlantic during the last glacial cycle. *Geology*, *40*(2), 123–126. https://doi.org/10.1130/G32779.1

Holzer, M., & Brzezinski, M. A. (2016). Controls on the silicon isotope distribution in the ocean: New diagnostics from a data-constrained model. *Global Biogeochemical Cycles*, *29*, 267–287. https://doi.org/10.1002/2014GB004967

Horn, M., Beucher, C. P., Robinson, R. S., & Brzezinski, M. A. (2011). Southern ocean nitrogen and silicon dynamics during the last deglaciation. *Earth and Planetary Science Letters*, *310*, 334–339. https://doi.org/10.1016/j.epsl.2011.08.016

Hülse, D., Arndt, S., Wilson, J. D., Munhoven, G., & Ridgwell, A. (2017). Understanding the causes and consequences of past marine carbon cycling variability through models. *Earth-Science Reviews*, *171*, 349–382. https://doi.org/10.1016/j.earscirev.2017.06.004

Hutchins, D. A., & Bruland, K. W. (1998). Iron-limited diatom growth and Si:N uptake ratios in a coastal upwelling regime. *Nature*, *393*, 561–564. https://doi.org/10.1038/31203

Jaccard, S. L., & Galbraith, E. D. (2011). Large climate-driven changes of oceanic oxygen concentrations during the last deglaciation. *Nature Geoscience*, *5*, 151–156. https://doi.org/10.1038/NGEO1352

Jaccard, S. L., Galbraith, E. D., Martínez-García, A., & Anderson, R. F. (2016). Covariation of deep Southern Ocean oxygenations and atmospheric CO_2 through the last ice age. *Nature*, *530*, 207–210. https://doi.org/10.1038/nature16514

Kamatani, A. (1992). Dissolution rates of silica from diatoms decomposition at various temperatures. *Marine Biology*, *68*, 91–96.

Knutti, R., Furrer, R., Tebaldi, C., Cermak, J., & Meehl, G. A. (2009). Challenges in combining projections from multiple climate models. *Journal of Climate*, *23*, 2739–2758. https://doi.org/10.1175/2009JCLI3361.1

Kohlfeld, K. E., Graham, R. M., de Boer, A. M., Sime, L. C., Wolff, E. W., Le Quéré, C., & Bopp, L. (2013). Southern Hemisphere westerly wind changes during the Last Glacial Maximum: Paleo-data synthesis. *Quaternary Science Reviews*, *68*, 76–95. https://doi.org/10.1016/j.quascirev.2013.01.017

Kriest, I., & Oschlies, A. (2008). On the treatment of particulate organic matter sinking in large-scale models of marine biogeochemical cycles. *Biogeosciences*, *5*, 55–72. https://doi.org/10.5194/bg-5-55-2008

Lagarias, J. C., Reeds, J. A., Wright, M. H., & Wright, P. E. (1998). Covergence properties of the Nelder–Mead simplex method in low dimensions. *SIAM Journal on Optimization*, *9*(1), 112–147. https://doi.org/10.1137/S1052623496303470

Locarnini, R. A., Mishonov, A. V., Antonov, J. I., Boyer, T. P., Garcia, H. E., Baranova, O. K., et al. (2010). World ocean atlas 2009, volume 1: Temperature. In S. Levitus (Ed.), *NOAA atlas NESDIS 68* (pp. 184). Washington, DC.: U.S. Government Printing Office.

Löptien, U., & Dietze, H. (2015). Constraining parameters in marine pelagic ecosystem models—Is it actually feasible with typical observations of standing stocks? *Ocean Science*, *11*(4), 573–590. https://doi.org/10.5194/os-11-573-2015

Löptien, U., & Dietze, H. (2017). Effects of parameter indeterminacy in pelagic biogeochemical modules of Earth System Models on projections into a warming future: The scale of the problem. *Global Biogeochemical Cycles*, *31*(7), 1155–1172. https://doi.org/10.1002/2017GB005690

Löptien, U., & Dietze, H. (2019). Reciprocal bias compensation and ensuing uncertainties in model-based climate projections: Pelagic biogeochemistry versus ocean mixing. *Biogeosciences*, *16*, 1865–1881. https://doi.org/10.5194/bg-16-1865-2019

Matsumoto, K., Chase, Z., & Kohfeld, K. (2014). Different mechanisms of silicic acid leakage and their biogeochemical consequences. *Paleoceanography*, *29*, 238–254. https://doi.org/10.1002/2013PA002588

Matsumoto, K., & Sarmiento, J. L. (2008). A corollary to the silicic acid leakage hypothesis. *Paleoceanography*, *23*, PA2203. https://doi.org/10.1029/2007PA001515

Matsumoto, K., Sarmiento, J. L., & Brzezinski, M. A. (2002). Silicic acid leakage from the Southern Ocean: A possible explanation for glacial atmospheric pCO_2. *Global Biogeochemical Cycles*, *16*(3), 1031. https://doi.org/10.1029/2001GB001442

McGee, D., Broecker, W. S., & Winckler, G. (2010). Gustiness: The driver of glacial dustiness? *Quaternary Science Reviews*, *29*(17-18), 2340–2350. https://doi.org/10.1016/j.quascirev.2010.06.009

Members, MargoProject (2009). Constraints on the magnitude and patterns of ocean cooling at the Last Glacial Maximum. *Nature Geoscience*, *2*, 127–132. https://doi.org/10.1038/NGEO411

Meyerink, S., Ellwood, M. J., Maher, W., & Strzepek, R. (2017). Iron availability influences silicon isotope fractionation in two Southern Ocean diatoms (Proboscia inermis and Eucampia Antarctica) and a coastal diatom (Thalassiosira pseudonana). *Frontiers in Marine Science*, *4*, 217. https://doi.org/10.3389/fmars.2017.00217

Moore, J. K., Fu, W., Primeau, F., Britten, G. L., Lindsay, K., Long, M., et al. (2018). Sustained climate warming drives declining marine biological productivity. *Science*, *359*(6380), 1139–1143. https://doi.org/10.1126/science.aao6379

Notz, D. (2015). How well must climate models agree with observations? *Philosophical Transactions of the Royal Society A.*, *373*(2052), 20140164. https://doi.org/10.1098/rsta.2014.0164

Opfergelt, S., Burton, K. W., Pogge von Strandmann, P. A. E., Gislason, S. R., & Halliday, A. N.(2013). Riverine silicon isotope variations in glaciated basaltic terrains: Implications for the Si delivery to the ocean over glacial-interglacial intervals. *Earth and Planetary Science Letters*, *369–370*, 211–219. https://doi.org/10.1016/j.epsl.2013.03.025

Peltier, W. R. (1994). Ice age paleotopography. *Science*, *265*(5169), 195–201. https://doi.org/10.1126/science.265.5169.195

Pichevin, L. E., Reynolds, B. C., Ganeshram, R. S., Cacho, I., Pena, L., Keefe, K., & Ellam, R. M. (2009). Enhanced carbon pump inferred from relaxation of nutrient limitation in the glacial ocean. *Nature*, *459*, 1114–1117. https://doi.org/10.1038/nature08101

Pondaven, P., Ruiz-Pino, D., Fravalo, C., Tréguer, P., & Jeandel, C. (2000). Interannual variability of *Si* and *N* cycles at the time-series station KERFIX between 1990 and 1995—A 1-D modelling study. *Deep Sea Research I*, *47*, 223–257. https://doi.org/10.1016/S0967-0637(99)00053-9

Ragueneau, O., Tréguer, P., Leynaert, A., Anderson, R. F., Brzezinski, M. A., DeMaster, D. J., et al. (2000). A review of the Si cycle in the modern ocean: Recent progress and missing gaps in the application of biogenic opal as a paleoproductivity proxy. *Global and Planetary Change*, *26*(4), 317–365. https://doi.org/10.1016/S0921-8181(00)00052-7

Reynolds, B. C. (2009). Modeling the modern marine δ^{30}Si distribution. *Global Biogeochemical Cycles*, *23*, GB2015. https://doi.org/10.1029/2008GB003266

Reynolds, B. C., Frank, M., & Halliday, A. N. (2006). Silicon isotope fractionation during nutrient utilization in the North Pacific. *Earth and Planetary Science Letters*, *244*, 431–443. https://doi.org/10.1016/j.epsl.2006.02.002

Schoelynck, J., Subalusky, A. L., Struyf, E., Dutton, C. L., Unzué-Belmonte, D., Van de Vijver, B., et al. (2019). Hippos (Hippopotamus amphibius): The animal silicon pump. *Science Advances*, *5*(5), 1–10. https://doi.org/10.1126/sciadv.aav0395

Sime, L. C., Kohfeld, K. E., Le, Quéré, Wolff, E. W., de Boer, A. M., Graham, R. M., & Bopp, L. (2013). Southern Hemisphere westerly wind changes during the Last Glacial Maximum: Model-data comparison. *Quaternary Science Reviews*, *64*, 104–120. https://doi.org/10.1016/j.quascirev.2012.12.008

Stoll, H. (2020). 30 years of the iron hypothesis of ice ages. *Nature*, *578*, 370–371. https://doi.org/10.1038/d41586-020-00393-x

Sutton, J. N., André, L., Cardinal, D., Conley, D. J., de Souza, G. F., Dean, J., et al. (2018). A review of the stable isotope bio-geochemistry of the global silicon cycle and its associated trace elements. *Frontiers in Earth Science*, *5*, 112. https://doi.org/10.3389/feart.2017.00112

Sutton, J. N., Varela, D. E., Brzezinski, M. A., & Beucher, C. P. (2013). Species-dependent silicon isotope fractionation by marine diatoms. *Geochimica et Cosmochimica Acta*, *104*, 300–309. https://doi.org/10.1016/j.gca.2012.10.057

Tréguer, P. J., & De La Rocha, C. L. (2013). The world ocean silica cycle. *Annual Review of Marine Science*, *5*, 477–501. https://doi.org/10.1146/annurev-marine-121211-172346

Tréguer, P., Nelson, D. N., Van Bennekom, A. J., DeMaster, D. J., Leynaert, A., & Quéguiner, B. (1995). The silica balance in the world ocean: A reestimate. *Science*, *268*(5209), 375–379. https://doi.org/10.1126/science.268.5209.375

Weaver, A. J., Eby, M., Wiebe, E. C., Bitz, C. M., Duffy, P. B., Ewen, T. L., et al. (2001). The UVic Earth System Climate Model: Model description, climatology, and applications to past, present and future climates. *Atmosphere-Ocean*, *39*, 361–428. https://doi.org/10.1080/07055900.2001.9649686

Wischmeyer, A. G., De La Rocha, C., Maier-Reimer, E., & Wolf-Gladrow, D. A. (2003). Control mechanisms for the oceanic distribution of silicon isotopes. *Global Biogeochemical Cycles*, *17*(3), 1083. https://doi.org/10.1029/2002GB002022